

# LES of Perfectly-Expanded Supersonic Jets Using an Unstructured Solver\*

S. Mendez <sup>†</sup> M. Shoeybi <sup>‡</sup> A. Sharma <sup>§</sup> F. E. Ham <sup>¶</sup> S. K. Lele <sup>||</sup> P. Moin <sup>\*\*</sup>

*Stanford University, Stanford, CA, 94305, USA*

## Abstract

Large-eddy simulations of supersonic jets are performed to validate the development of a second-order finite volume unstructured solver for aeroacoustic applications. Two supersonic jets issuing from an axisymmetric nozzle at Mach number 1.4 are computed: one unheated jet with a Reynolds number of 150,000 and one heated jet with a Reynolds number of 76,000 and a temperature ratio of 1.75. Flow and noise results are compared with the experimental database from NASA Glenn Research Center. The nozzle is included in the computational domain. The present study shows that the results from the unstructured solver are in good agreement with the experimental data for time-averaged and fluctuating quantities, velocity spectra in the jet, and the sound obtained in the near field and the far field using the integration of the Ffowcs-Williams and Hawkings equation.

## Nomenclature

$c$	Sound speed
$D$	Nozzle exit diameter
$f$	Sampling frequency

---

\*A first version of this article was presented at the 48th AIAA Aerospace Sciences Meeting, as AIAA-2010-271.

<sup>†</sup>Post-doctoral Fellow, Department of Mechanical Engineering; smendez@stanford.edu. Current address: University Montpellier II. I3M, UMR CNRS 5149. smendez@univ-montp2.fr.

<sup>‡</sup>Graduate Student, Department of Mechanical Engineering. Current address: Cascade Technologies Inc., Palo Alto, CA

<sup>§</sup>Graduate Student, Department of Mechanical Engineering

<sup>¶</sup>Research Associate, Department of Mechanical Engineering

<sup>||</sup>Professor, Department of Mechanical Engineering & Department of Aeronautics and Astronautics

<sup>\*\*</sup>Professor, Department of Mechanical Engineering

$\vec{F}$	Navier-Stokes fluxes operator
$F_1, F_2$	Source terms in the FWH integration
$\vec{G}$	Subgrid fluxes operator
$M$	Mach number
$M_a$	Acoustic Mach number $M_a = U_j/c_\infty$
$n_i$	$i$ th component of the unit vector normal to the FWH surface
$NPR$	Nozzle pressure ratio
$p$	Pressure
$p'$	Pressure fluctuations relative to the ambient pressure $p' = p - p_\infty$
$p_{ref}$	Reference pressure $p_{ref} = 2 \times 10^{-5} Pa$
$\vec{q}$	Vector of state variables
$q_i^{sgs}$	$i$ th component of the subgrid heat flux
$r_j$	$j$ th component of the unit vector from the surface element location to the observer location in the FWH calculation
$r$	Generally, radial coordinate. In the FWH calculation, distance from the surface element location to the observer location
$R$	Nozzle exit radius, $R = D/2$
$Re$	Reynolds number $Re = \rho_j U_j D / \mu_j$
$S_{ij}$	Strain rate tensor
$ S $	Magnitude of strain rate tensor
$St$	Strouhal number $St = \omega D / 2\pi U_j$
$St_{max}$	Nyquist Strouhal number $St = f D / 2 U_j$
$St_{min}$	Minimum Strouhal number $St = D / \tau U_j$
$t$	time
$t_0$	Characteristic time $t_0 = R / c_\infty$
$T$	Temperature
$TR$	Temperature ratio $TR = T_j / T_\infty$
$u$	Streamwise velocity, i.e. $u_1$
$u_i$	$i$ th component of the velocity vector
$u_n$	Velocity normal to the surface element location in the FWH calculation $u_n = u_i n_i$
$U$	Time-averaged streamwise velocity
$v$	Radial velocity
$w$	Azimuthal velocity
$\vec{x}$	Surface element location in the FWH calculation
$\vec{y}$	Observer location in the FWH calculation
$x_i$	$i$ th component of the coordinates vector
$x$	Streamwise coordinate, i.e. $x_1$

$y$	Vertical coordinate, i.e. $x_2$
$z$	Spanwise coordinate, i.e. $x_3$
$\alpha$	Artificial dissipation coefficient
$\delta_\theta$	Momentum thickness of the boundary layer at the nozzle exit
$\delta_{ij}$	Kronecker symbol
$\Delta$	LES filter width
$\Delta r$	Grid resolution in the radial direction
$\Delta t$	Time step size
$\Delta x$	Grid resolution in the axial direction
$\mu$	Dynamic viscosity
$\omega$	Angular frequency
$\rho$	Density
$\tau_{ij}^{sgs}$	Subgrid stress tensor
$\tau$	Accumulation time
<i>Subscript</i>	
$j$	Relative to the jet at the nozzle exit
$\infty$	Relative to the ambient conditions
$rms$	Root Mean Square (RMS) value
<i>Superscript</i>	
$sgs$	Relative to the subgrid model
$*$	Complex conjugate
<i>Operators</i>	
$\hat{\cdot}$	Fourier transform: e.g. $(\hat{p}(\omega) = \int_{-\infty}^{\infty} p(t)e^{-i\omega t} dt)$
$\bar{\cdot}$	Subgrid filtering

## I. Introduction

Large-eddy simulation (LES) has the potential to become a tool of choice to perform predictions of the noise generated by turbulent jets.<sup>1</sup> It does not have the same limitation in Reynolds number as Direct Numerical Simulation and can thus handle values of Reynolds number more relevant to industrial applications. From the physical point of view, LES is well suited to jet noise computations, because important contribution to jet noise comes from the local largest scales of the turbulent flows,<sup>2-4</sup> for which Reynolds-Averaged Navier-Stokes methods fail to provide a good description in the general case.

From the first studies,<sup>5,6</sup> LES for jet noise application has been tremendously developed.<sup>1</sup> Different numerical approaches have been tested<sup>1,7-15</sup> but generally, high-order finite differ-

ence methods are used. These methods are chosen for their resolution properties in terms of dissipation and dispersion, which are essential features for aeroacoustic predictions.<sup>16</sup> A promising method is the one used by Shur, Spalart and Strelets and co-workers.<sup>8,17-20</sup> Coupling a multi-block structured finite difference solver with a Ffowcs Williams-Hawkings (FWH) integration, their method was able to provide satisfactory noise results, generally with an accuracy of 2-3 dB, on a wide range of operating conditions<sup>17</sup> and in non-axisymmetric cases,<sup>18,20</sup> including chevrons.

However, their simulations with chevrons do not include the chevrons and use an emulation procedure, with sources and sinks with a zero net mass flux. This procedure yields reasonable results, but is of course limited. Spalart, Shur and Strelets<sup>19</sup> state that geometric complexities cannot be handled without developing unstructured-grid solvers. Indeed, the interest for unstructured solvers has increased in the jet noise community over the last years. Studies deal with geometrical configurations of an increasing complexity and sometimes present promising results<sup>10</sup> in very complex cases.

A wide range of numerical approaches are used for jet noise computations on unstructured grids. Most groups rely on finite-volume solvers,<sup>10,21-26</sup> based either on a cell-vertex<sup>22,23</sup> or a cell-centered scheme.<sup>10,21,23,24</sup> Numerical schemes for spatial discretization are diverse: authors report either third-order upwind scheme,<sup>25,26</sup> second-order MUSCL,<sup>24</sup> or schemes<sup>10,22,23</sup> based on the flux difference ideas developed by Roe.<sup>27</sup> A finite-element version of the flux-corrected transport (FCT) algorithm is used for supersonic jet studies by Liu *et al.*<sup>15,28</sup> Preliminary studies using a linear discontinuous Galerkin solver have also been presented.<sup>29</sup> Generally, authors use hexahedral meshes.<sup>10,23,26</sup> Liu *et al.*<sup>15,28</sup> and Lupoglazoff *et al.*<sup>25</sup> use tetrahedral grids, but the latter show very dissipative simulations using tetrahedral elements. Consequently, they prefer hybrid grids with hexahedral elements in the mixing layer.<sup>24,25</sup> In terms of subgrid-scale modeling, the most common approach is to rely on the numerical dissipation by the scheme, without any subgrid-scale model.<sup>10,15,22-26,28</sup> Explicit subgrid-scale models are rarely used,<sup>21,29,30</sup> and no consensus is reached about which model is better. When far-field noise is computed, LES solvers are generally coupled with the FWH integral method.<sup>10,23,26</sup> This strategy does not require resolving the acoustic far field, as the wave propagation is handled analytically, which is particularly interesting when using low-order numerical schemes. Overall, this literature review shows that there is no consensus about a preferred approach to perform unstructured LES for jet noise.

Although promising results are often shown, studies deal with more and more complex configurations without providing enough validation on simple cases. Numerous publications are indeed feasibility studies. LES of dual-stream nozzles,<sup>22,24</sup> or chevron nozzles<sup>10,15,24</sup> are published, however their results on simple round jets do not seem to be validated enough. Indeed, numerical results are sometimes open to questions: *e.g.* apart from the publications

by Tucker and co-workers<sup>10,22,23</sup> and Khalighi *et al.*,<sup>30,31</sup> instantaneous solutions from unstructured solvers do not show the turbulent aspect expected in high-speed jets. Small eddies are often missing in the jet, especially near the nozzle.<sup>15,21,24–26,28</sup> It is unclear if this is due to the use of thick incoming boundary layers or dissipative solvers. Publications generally compare computational root mean square values of velocity fluctuations with experimental data, showing reasonable agreement. However, experimental and computed velocity spectra would probably differ. When presented, noise results are often insufficiently detailed (or validated) to judge the quality of the predictions.

This short review shows that there is a large variety of unstructured approaches available, none of which provides as extensive and validated results as the ones corresponding to the state of the art with structured solvers. In addition, in numerous publications, the instantaneous velocity fields presented suggest that the numerical method used is quite dissipative, which should be corrected to obtain accurate high-frequency noise predictions. Finally, any method developed should be extensively validated, presenting flow, noise, integrated data and spectra to allow to judge its capability as clearly as possible.

The study reported here can be considered as the early stages of the development of an unstructured solver for complex realistic LES of supersonic jet noise for industrial applications. As stated before, recent LES for jet noise prediction using unstructured solvers often rely on low-order dissipative schemes and implicit dissipation instead of explicit subgrid scale models. The approach chosen here is different: using a second-order low-dissipation scheme, it is possible to use explicit subgrid-scale and shock-capturing models and thus control more precisely the dissipation introduced by the method. The LES solver is coupled with a FWH integration to calculate the far-field noise. The objective of this paper is to carefully evaluate the capability of the unstructured solver to predict the noise generated by supersonic jets. Such a study has also been carried out by Shoeybi<sup>32</sup> with the same numerical method for subsonic jets, showing quantitative comparisons with experiments for both flow and noise.

As the experience in using unstructured LES solvers for supersonic jet noise is still limited, an analysis of the solver capabilities in simple, well-documented cases is needed. Supersonic round jets, issuing from an axisymmetric nozzle, are computed. The jet flows considered have a minimal pressure mismatch, to remove as much as possible shock-associated noise (broadband shock noise and screech). The present study demonstrates a thorough validation of the unstructured flow solver for jet noise applications. The experimental database generated recently by Bridges and Wernet<sup>33</sup> is used to validate the jet noise computations. It is presented in section II. After the presentation of the numerical method in section III, the numerical setup is detailed in section IV. LES results for the supersonic jets are presented and compared to experimental data in section V.

## II. Experimental configuration of interest and operating conditions

Two almost perfectly-expanded jet flows, one unheated and one heated, are considered in this study. Both simulated jet flows correspond to the converging-diverging SMC015 nozzle studied by Bridges and Wernet<sup>33</sup> and designed by the method of characteristics to obtain fully expanded jets at exit Mach number 1.4. The nozzle diameter at the exit is  $D = 5.08 \cdot 10^{-2}$  m. The length of the nozzle is  $7.55 D$ . Its initial diameter is  $3 D$ , so that the area contraction between the nozzle inlet and the nozzle exit is 9:1. The throat of the nozzle is located at  $x = -0.93 D$ . The cross-section area at the throat is approximately 90% of the exit area. The nozzle lip has sharp edges and the lip thickness is  $0.015 D$ . The geometry can be seen in Fig. 2(a).

Two operating points are considered in this study, corresponding to an isothermal jet and a heated jet. Both cases result in the same jet Mach number  $M_j \approx 1.4$ . The heated jet issues from the nozzle at a higher temperature than the ambient medium: the target temperature ratio is  $TR = 1.765$ . To keep the same Mach number as in the isothermal case, the jet velocity is higher in the heated case. The Reynolds number is of order of  $10^6$  for the two cases. The ambient medium is at rest and its conditions are identical in both cases. However, the experimental Mach number for which minimal shocks are obtained does not match exactly the design Mach number.<sup>33</sup> Furthermore, from one data set to another in the experimental database, conditions slightly vary. The conditions of the data set used for comparison against the LES results are the following: for the unheated jet,  $M_j = 1.382$ ,  $TR = 0.997$  and  $NPR = 3.14$ . For the heated jet,  $M_j = 1.386$ ,  $TR = 1.749$  and  $NPR = 3.12$ . The acoustic Mach number is  $M_a = 1.833$ .

The experimental data sets from the NASA SHJAR test rig<sup>33,34</sup> were provided by Dr. James Bridges. Flow results are measured using particle image velocimetry (PIV). Experimental data is usually acquired at a sample rate of 25 kHz. The associated Nyquist Strouhal number is 1.4 for the unheated case and 1.0 for the heated case. PIV measurements may be plagued by various errors,<sup>35</sup> especially near the nozzle. A quality index was provided together with the experimental PIV measurements. Along the centerline, the quality index is high, and results are displayed downstream of  $x = 0.25 D$ . Along the lip line and very close to the nozzle, the quality of the PIV results is lower (see additional comments in appendix B). Measurements upstream of  $x = D$  had to be discarded. Noise measurements are acquired at a sample rate of 200 kHz. The SHJAR database contains extensive flow and noise measurements: several experimental campaigns were led using the same geometry, with the same operating conditions. As a consequence, numerous different measurements are available. However, the drawback is that all measurements used here were not obtained

during the same tests. Experimental conditions may vary slightly from one test to another. These differences are pointed out in the paper wherever needed.

### III. Numerical approach: description of the LES flow solver and of the FWH solver

#### A. Numerical approach: hybrid implicit-explicit LES solver

A compressible LES solver called ‘CDP-C’ is used. CDP-C has a fully compressible formulation based on a hybrid implicit-explicit numerical scheme.<sup>32,36</sup> The conservative density, momentum, and total energy equations are discretized using a second-order finite-volume cell-vertex scheme on an unstructured mesh. The formulation is equipped with minimal dissipation by adopting summation-by-parts (SBP) operators<sup>37</sup> for unstructured grids, along with the simultaneous approximation term (SAT) method<sup>38,39</sup> for imposing boundary conditions. The SBP operators are skew-symmetric and are energy-conserving for linear problems. The SBP/SAT combination leads to a linearly stable semi-discrete scheme.<sup>32,36</sup>

An important feature of CDP-C is the hybrid implicit-explicit time advancement scheme; the code automatically identifies the stiff terms in the governing equations and treats them implicitly. This leads to significant savings in the computational time and memory allocation compared to fully implicit or fully explicit schemes. This method is particularly well adapted for compressible jet simulations where the nozzle is included in the domain. The region of very fine grid used near the walls and in the early development of the shear layer is treated implicitly, while an explicit time advancement is used in the major part of the computational domain.

Small-scale turbulence is modeled using the dynamic modeling procedure of Moin *et al.*<sup>40</sup> with Lilly’s modification.<sup>41</sup> The accuracy and robustness of the numerical formulation have been tested against a wide range of canonical flows, such as compressible isotropic turbulence and subsonic and transonic turbulent flow over a cylinder.<sup>32,36</sup>

#### B. Artificial dissipation

Numerical computations often require artificial dissipation to remove unphysical high-frequency oscillations. These unphysical oscillations are especially present in the regions with low-quality grid cells, for which the discretization operators are less accurate. In order to reduce the spurious oscillations, the fourth-order stable artificial dissipation of Svård *et al.*<sup>42</sup> is added to the governing equations, to damp the under-resolved high-wavenumber oscilla-

tions. Consider the Navier-Stokes equations in the form,

$$\frac{\partial \vec{q}}{\partial t} + \vec{F}(\vec{q}) = 0, \quad (1)$$

where  $\vec{q}$  contains state variables (density, momentum and total energy). The artificial dissipation of Svärd *et al.*<sup>42</sup> modifies the equations as:

$$\frac{\partial \vec{q}}{\partial t} + \vec{F}(\vec{q}) = -\alpha \tilde{\nabla}^4 \vec{q} \quad (2)$$

where  $\alpha$  is a positive constant, of dimension  $\text{m}^4\text{s}^{-1}$  and  $\tilde{\nabla}^4$  is the 4<sup>th</sup> order undivided polyharmonic operator of Svärd *et al.*<sup>42</sup> In the simulations,  $\alpha = 10^{-3} \text{ m}^4\text{s}^{-1}$ . This dissipation will not alter the order of accuracy of the scheme and will preserve the stability of the numerical method. Furthermore, fourth-order dissipation will be mostly present at high wavenumbers and therefore it will be less effective to the resolved scales. Higher order dissipation requires a larger stencil and therefore will be more expensive.

Note that turbulent flows are sensitive to artificially added numerical dissipation.<sup>43</sup> Therefore, the artificial dissipation should be managed carefully such to minimize its effect on the resolved flow structures. In a former publication,<sup>44</sup>  $\alpha$  was made variable in space in order to minimize the artificial dissipation added over the fully turbulent part of the jet, where the subgrid model is active. Decreasing  $\alpha$  was shown to increase the high-frequency sound obtained (typical increase of 1 dB for  $St > 1$  was obtained for upstream angles), albeit without changing the results qualitatively. However, the present work uses a constant artificial dissipation coefficient and does not study the effect of a variable  $\alpha$ .

### C. Subgrid model

Recalling the Navier-Stokes equations:

$$\frac{\partial \vec{q}}{\partial t} + \vec{F}(\vec{q}) = 0, \quad (3)$$

the LES equations can be written as (for details see Nagarajan *et al.*<sup>45</sup>)

$$\frac{\partial \vec{q}}{\partial t} + \vec{F}(\vec{q}) = \vec{G}(\vec{q}, \vec{q}), \quad (4)$$

where  $\vec{G}(\vec{q}, \vec{q})$  is the subgrid flux and has the form  $[0, \frac{\partial \tau_{ij}^{sgs}}{\partial x_j}, \frac{q_j^{sgs}}{\partial x_j}]^T$ . These subgrid terms are modeled using the Smagorinsky model as:

$$\tau_{ij}^{sgs} - \frac{1}{3} \tau_{kk}^{sgs} \delta_{ij} = 2C \bar{\rho} \Delta^2 |\bar{S}| (\bar{S}_{ij} - 1/3 \bar{S}_{kk} \delta_{ij}), \quad (5)$$

$$\tau_{kk}^{sgs} = 2C_I \bar{\rho} \Delta^2 |\bar{S}|^2, \quad (6)$$

$$q_i^{sgs} = -\frac{C \bar{\rho} \Delta^2 |\bar{S}|}{Pr_t} \frac{\partial \bar{T}}{\partial x_i}. \quad (7)$$

Note that coefficients  $C$ ,  $C_I$ , and  $Pr_t$  are computed dynamically using dynamic procedure of Moin *et al.*<sup>40</sup> with the modification proposed by Lilly.<sup>41</sup> An azimuthal filter combined with a top hat filter over 5 points is used to smooth the field of eddy viscosity. Note that due to stability problems, it is assumed that  $\tau_{kk}^{sgs} = 0$ .

#### D. Shock-capturing method

The artificial bulk viscosity method<sup>46</sup> in a generalized form is used to capture shock waves on unstructured grids in CDP-C code. This model has further been improved by Mani *et al.*<sup>47</sup> to minimize the effect of artificial bulk viscosity on turbulence as well as dilatational motions. In the CDP-C solver, the model has been adapted for unstructured grids.<sup>32</sup> Notably, the proposed model scales properly with the mesh resolution regardless of the local grid alignment.

#### E. Ffowcs Williams-Hawkings solver

Due to high computational cost of direct simulations, far-field evaluation of sound requires the use of hybrid methods. Hybrid methods rely on direct simulation for near field acoustic source data (here from the LES solver) and projection of this data to the far field. The advantage is that expensive direct non-linear calculation of the flow is needed only for the near field. In this work, the frequency domain permeable surface FWH formulation is used,<sup>48</sup> already described in detail by Mendez *et al.*<sup>49</sup> A FWH surface  $S$  enclosing the jet is defined (a typical FWH surface is shown in Fig. 1). The surface first follows the shape of the nozzle, then more or less follows the growth of the jet, the section increasing downstream. The surface used is open at the inflow, but this has no consequence on the calculated sound because the inflow is quiet. A vertical outflow disk is located downstream, crossing the jet and the surface is thus closed at its downstream end.

The volume integral of the original FWH equation, representing the noise radiated by quadrupoles located outside the surface, is omitted. This would be exact only if all noise sources were entirely enclosed inside the FWH surface. Due to the very long turbulent region in high-speed jets, this is not possible in the calculations. One of the challenges is to minimize the errors due to the use of the inexact FWH formulation. With this goal in mind, extensive tests were performed and presented in a former publication.<sup>49</sup> The procedure employed to calculate the far-field sound in the present article, which resulted in the smallest errors in former tests, is summarized in the present section.

The time history of conservative variables is stored over a given surface  $S$  (referred to as FWH surface) at a specified sampling frequency  $f$  and for a total time  $\tau$ .  $f$  is associated with the Nyquist Strouhal number  $St_{max} = f D/2U_j$ .  $\tau$  determines the minimum frequency accessible by this post-processing  $St_{min} = D/\tau U_j$ . Note that tests<sup>49</sup> showed that for Strouhal numbers smaller than  $10 St_{min}$ , results are not perfectly converged in time.

For each surface element of  $S$ , the time history of source terms  $F_1$  and  $F_2$  are constructed from the conservative variables using the following expressions:

$$F_1 = \frac{p'n_j r_j + \rho u_j u_n r_j}{c_\infty r} + \frac{\rho u_n}{r} \quad \text{and} \quad F_2 = \frac{p'n_j r_j + \rho u_j u_n r_j}{r^2}. \quad (8)$$

$n_j$  is the  $j$ th component of the unit surface normal vector, and  $r$  and  $r_j$  represent the magnitude and the direction of the vector from the surface element location  $\vec{y}$  to the observer location  $\vec{x}$ . Note that the effect of viscous stresses has been neglected. In the original formulation,<sup>48</sup>  $\rho$  is the density. Another formulation, based on pressure, is used here.<sup>50,51</sup> In the absence of volume integral, the only difference with the original formulation is that  $\rho = \rho_\infty + p'/c_\infty^2$ . In hot jets,  $\rho'$  is significantly higher than  $p'/c_\infty^2$  on the outflow disk due to important entropy fluctuations. Using the pressure formulation thus decreases the spurious sound generated by the passage of turbulent eddies through the outflow disk.

$F_1$  and  $F_2$  are then windowed using Hanning windowing after subtracting the mean, and time-Fourier-transformed. The time derivative of  $F_1$  is calculated in the frequency space. The retarded time ( $\exp(-i\omega r/c_\infty)$ ) is also applied in the frequency space. The integral of the source terms over the surface then yields the Fourier transform of the pressure at the observer location:

$$4\pi\hat{p}(\vec{x}, \omega) = \int_S i\omega \hat{F}_1(\vec{y}, \omega) \exp(-i\omega r/c_\infty) d\vec{y} + \int_S \hat{F}_2(\vec{y}, \omega) \exp(-i\omega r/c_\infty) d\vec{y}. \quad (9)$$

The Narrowband Sound Pressure Level ( $SPL$ ) level (in dB) is calculated as:

$$SPL(\vec{x}, St) = 10 \log_{10} \left( \frac{2\hat{p}(\vec{x}, \omega)\hat{p}^*(\vec{x}, \omega)}{St_{min} p_{ref}^2} \right). \quad (10)$$

and the Overall Sound Pressure Level ( $OASPL$ , in dB) is computed as

$$OASPL(\vec{x}) = 10 \log_{10} \left( \sum_{St=0}^{St_{max}} \frac{2\hat{p}(\vec{x}, \omega)\hat{p}^*(\vec{x}, \omega)}{p_{ref}^2} \right) \quad (11)$$

At the downstream end of the surface, several options were tested:<sup>49</sup> open surfaces (with no outflow disk) were shown to yield very high spurious sound at low frequencies. Errors due to the passage of eddies through a closed surface were smaller. Closed surfaces are

thus preferred. In order to further improve the closed-surface results, averaging over outflow disks is used. This technique was first used by Shur, Spalart and Strelets.<sup>8</sup> It consists of computing  $\hat{p}$  using Eq. (9) for several surfaces having the exact same shape, but with the outflow disks located at different streamwise positions. Results in  $\hat{p}$  from the different surfaces are then averaged. The spurious noise generated by the passage of turbulent eddies through the outflow disk is not in phase from one surface to another. It is thus partially or totally cancelled averaging is used. Details of the FWH surfaces used are provided in the following section.

## IV. Numerical setup

### A. Presentation of the calculations

Three computations are presented in this paper. S1 is the simulation of the unheated case and S2 and S3 represent the heated case. Physical and numerical parameters of runs S1 to S3 are provided in Table 1. The same grid, denoted by grid 1&2, is used for cases S1 and S2. S3 focuses on the same operating point as S2, using a second grid, denoted by grid 3. Grids are described in more details in the following section.

	$M_j$	$M_a$	$TR$	$Re$	$\delta_\theta/D$	$NPR$	grid	$\Delta tc_\infty/R$
S1	1.393	1.388	0.993	150,000	0.002	3.15	grid 1&2	0.005
S2	1.386	1.836	1.755	76,600	0.003	3.11	grid 1&2	0.005
S3	1.386	1.836	1.755	76,600	0.003	3.11	grid 3	0.005

Table 1: Operating conditions and numerical characteristics of the simulations considered. Notations are the following: the jet Mach number is  $M_j = U_j/c_j$ , the acoustic Mach number is  $M_a = U_j/c_\infty$ .  $\Delta tc_\infty/R$  is the non-dimensional time step.

### B. Computational domain, grids and FWH surface

The computational domain (size of the domain, geometry) is kept the same for all calculations. In Fig. 1, an instantaneous field of density from case S3 over the cutting plane  $z = 0$  is shown to present the computational domain. The origin ( $x=0$ ,  $y=0$ ,  $z=0$ ) is located at the center of the nozzle exit. As seen in Fig. 1, the nozzle is included in the computational domain. The computational domain extends up to  $x = 46.5 D$ . From  $x = 33 D$ , a sponge treatment (represented in Fig. 1 by a hatched zone) is applied to damp the turbulent fluctuations before they reach the outlet boundary. In the radial direction, the extension of the computational domain depends on the axial position. The radial size of the computational domain increases with the jet diameter. The domain (not the grid) is axisymmetric.

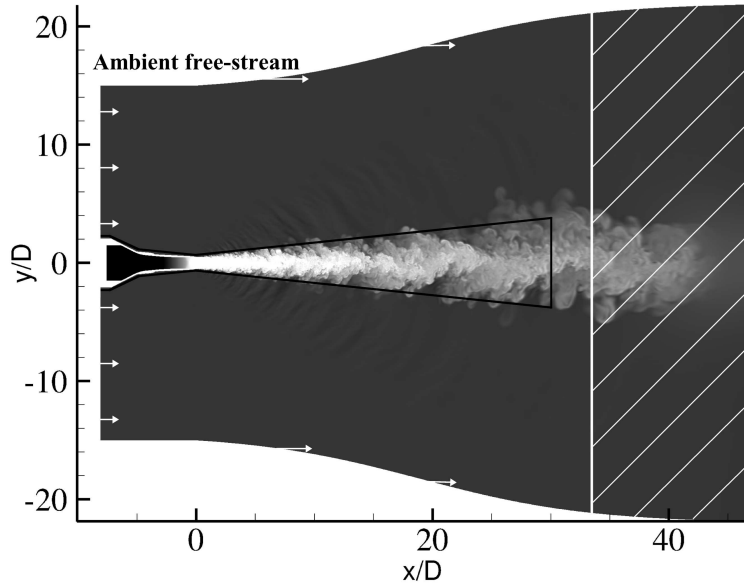


Figure 1: View of the computational domain (cutting plane  $z = 0$ ) with a density field from S3. The black line represents a typical location of the FWH surface (see details further). The hatched region, starting at the vertical white line, corresponds to the part of the domain where a sponge treatment is applied.

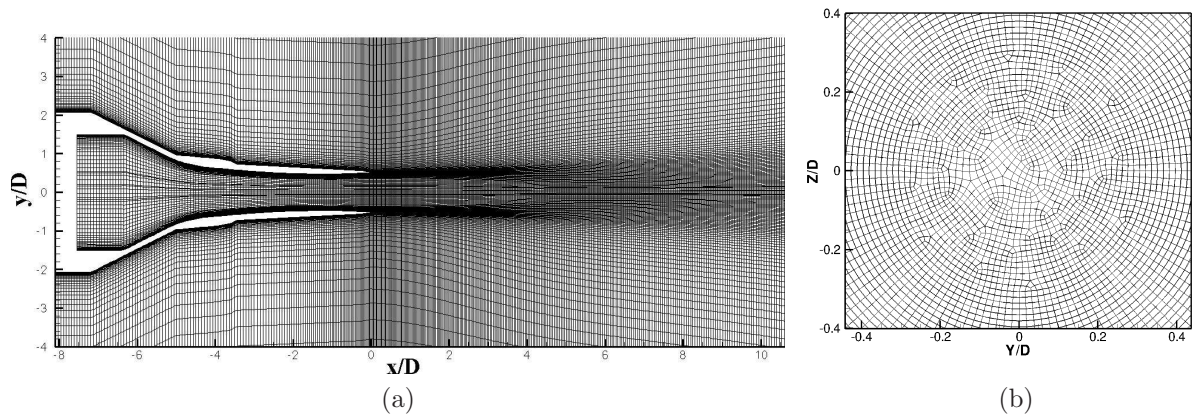


Figure 2: Grid used for the LES in cases S1 and S2. (a): Cutting plane  $z = 0$  through the center of the nozzle. Every second grid point is shown in both directions. (b): Cross section of the grid used for cases S1 and S2, at location  $x/D = 10$ .

The nozzle geometry can be seen in Fig. 2(a), together with the mesh corresponding to cases S1 and S2. As in most of the publications using unstructured solvers for LES of jet noise, hexahedral grids are used in this study, tetrahedral grids being found to be more diffusive.<sup>25,28</sup> The grid is made of two parts. In the center of the domain (small radii), the grid is an unstructured cylinder of variable radius. The radius of this unstructured core decreases from the inlet, reaches a minimum approximately at the end of the potential core then increases. Outside this unstructured core, a purely axisymmetric grid is used, with 128 points in the azimuthal direction. A cross section of the grid can be seen in Fig. 2(b). In the radial direction, the minimum grid spacing is used at the approximate location of the mixing layer between the jet and the ambient medium. In the grids used in this study, 8 points span the nozzle lip ( $\Delta r = 0.001875 D$  at  $r = 0.5 D$  and  $x = 0$ ). Grids are progressively stretched, both in the radial and the axial directions, to allow damping of the acoustic waves before they reach the boundaries of the mesh. It is also indispensable to keep the computational cost manageable.

Table 2 shows the grid resolution along the nozzle lip line. Compared to the grid used for S1 and S2 (grid 1&2), the grid used for S3 (grid 3) has been refined in the axial direction downstream of  $x = 11 D$ . Although the radial resolution for both grids are the same along the nozzle lip line, grid 3 is slightly refined in the radial direction at the edge of the jet for a better propagation of acoustic waves before they reach the FWH surface. Grid 1&2 contains 17 million cells and grid 3 contains 28 million cells.

$x/D$	$D/\Delta x$		$D/\Delta r$
	grid 1&2	grid 3	both grids
0	80	80	517
5	45	51	92
10	31	38	62
20	8	18	35
30	4	11	28

Table 2: Grid spacing along the nozzle lip line  $r/D = 0.5$  at different axial locations for grid used for S1 and S2 (grid 1&2) and the grid used for case S3 (grid 3).

No quantitative criterion can be found in the literature about how to define *a priori* the FWH surface. From the experience of former studies<sup>8,50</sup> and tests on the present cases,<sup>49</sup> a FWH surface has been defined: it is an axisymmetric surface following the exterior nozzle wall for  $x < 0$ . The surface is located at:

$$r/D = 0.75 + 0.1(x/D), \quad \text{for } 0 \leq x/D \leq x_{out}. \quad (12)$$

$x_{out}$  is the streamwise location of the outflow disk. For outflow disk averaging, 11 surfaces defined by Eq. (12) were used, with  $x_{out}$  located at  $25 D$ ,  $25.5 D, \dots, 30 D$ , respectively. The radial grid resolution at the FWH surface is presented in Table 3. It is also useful to present this information in terms of the highest frequency of sound waves locally supported by the grid. Under-resolution results in numerical errors dominated by dispersion errors, the phase velocity of under-resolved waves being under-predicted. 1-D tests of propagation of a sinusoidal periodic acoustic wave of small amplitude and 2-D tests reported by Shoeybi<sup>32</sup> have been performed. They have shown that the phase velocity of an acoustic wave is underestimated by 20% if the wavelength of the acoustic wave is only 8 times the grid spacing. It is chosen to be the minimum resolution requirement.  $St_{lim}$  is defined as the Strouhal number of an acoustic wave discretized by 8 points per wavelength at the FWH surface:  $St_{lim} = \frac{D/\Delta r}{8 M_a}$ . Values as a function of the axial coordinate are provided in Table 3. The grid cut-off Strouhal number is estimated to be twice  $St_{lim}$  (artificial dissipation rapidly dissipates acoustic waves represented over less than 4 grid points).

$x/D$		0	2.5	5	7.5	10	15	20	25	30
$D/\Delta r$	grid 1&2	48	32	28	24	22	20	18	16	14
	grid 3	66	43	38	33	30	27	24	21	19
$St_{lim}$	simulation S1	4.3	2.9	2.5	2.1	2.0	1.8	1.6	1.4	1.3
	simulation S2	3.2	2.2	1.9	1.6	1.5	1.4	1.2	1.1	1.0
	simulation S3	4.5	2.9	2.6	2.2	2.0	1.8	1.6	1.4	1.3

Table 3: Radial grid spacing along the FWH surface (defined by Eq. (12)), at different axial locations for grid used for S1 and S2 and the grid used for S3. A limit Strouhal number of acceptable resolution  $St_{lim}$  is estimated.

### C. Boundary conditions

Both the internal and external walls of the nozzle are non-slipping conditions. The experimental temperature of the nozzle walls is not known. Adiabatic and isothermal boundary conditions have been applied, without observing major changes in the results. The simulations presented in the paper use isothermal boundary conditions, at the temperature corresponding to flow (ambient temperature for the external surface of the nozzle, local jet temperature for the internal surface). At the nozzle inlet condition, a flat profile is imposed, with a hyperbolic tangent profile near the nozzle wall, of displacement thickness  $0.07 D$ , to reach zero velocity. Laminar inflow conditions are imposed. The grid used is not sufficiently fine for the flow to transition inside the nozzle.<sup>52</sup> The boundary layer at the nozzle exit is then laminar. Using thin boundary layers, it is however possible to obtain a rapid transition to turbulence once the jet exits from the nozzle.<sup>8,17</sup> This technique is popular as it does not

introduce forcing parameters in the calculation, while enabling the use of manageable grids. Bogey and Bailly<sup>53</sup> report a very interesting study of the impact of using laminar boundary layer on the flow and acoustic results of a Mach 0.9 jet.

In the experiment, the jet issues from the ambient nozzle in a medium at rest. To prevent any spurious recirculation and allow flow entrainment by the jet, a very slow flow (at Mach number 0.008) is imposed outside the nozzle. The thermodynamic characteristics of this external flow correspond to the ambient conditions. The radial boundary of the domain is treated in the same way. This makes the boundary conditions robust, notably by preventing changes of velocity signs at the free-stream boundary. An outflow boundary condition is applied downstream (on the right in Fig. 1).

In order to avoid any spurious reflection at the boundaries, a sponge treatment has been implemented. In the sponge region, a penalty term is applied on all resolved equations to lead the solution towards a target field. The sponge forcing term is increased gradually to be very small at the beginning of the sponge region ( $x = 33 D$ ) and high at the end, at the boundary ( $x = 46.5 D$ ). This enables the progressive dissipation of the vortices in the wake of the jet and of the acoustic waves before they reach the boundaries. This method is classical for aeroacoustic applications and parameters have been adjusted following the guidelines provided by ref. 27. In the present calculations, it is applied near the outlet boundary condition, on the last third of the computational domain (see Fig. 1).

#### D. Running procedure

Results are obtained using the following methodology: first calculations are driven to a statistically steady state on a coarse grid, typically twice as coarse in every direction as grid 1&2. The solution is then been interpolated on the fine grid. Jet simulations are run for a long time: typically, a particle released at the inlet condition needs 90 characteristic times  $t_0 = R/c_\infty$  to reach the nozzle exit. Typical convergence time after interpolation on fine grid is  $250 t_0$ . Averages are gathered over  $300 t_0$ . This would correspond to three to four flow through times (FTT), the FTT being defined as the time needed by a particle to go from the exit of the nozzle to the beginning of the sponge region, on the jet centerline (based on time-averaged velocity). The longest simulation (S3) was run on 768 processors using the Athena supercomputer (Cray XT4) at the National Institute for Computational Sciences (NICS). To gather statistics over  $300 t_0$  using a grid of 28 million cells, 96 hours (wall-clock time) were necessary, which approximately corresponds to 74,000 CPU hours.

## V. Results

### A. Overview of the results

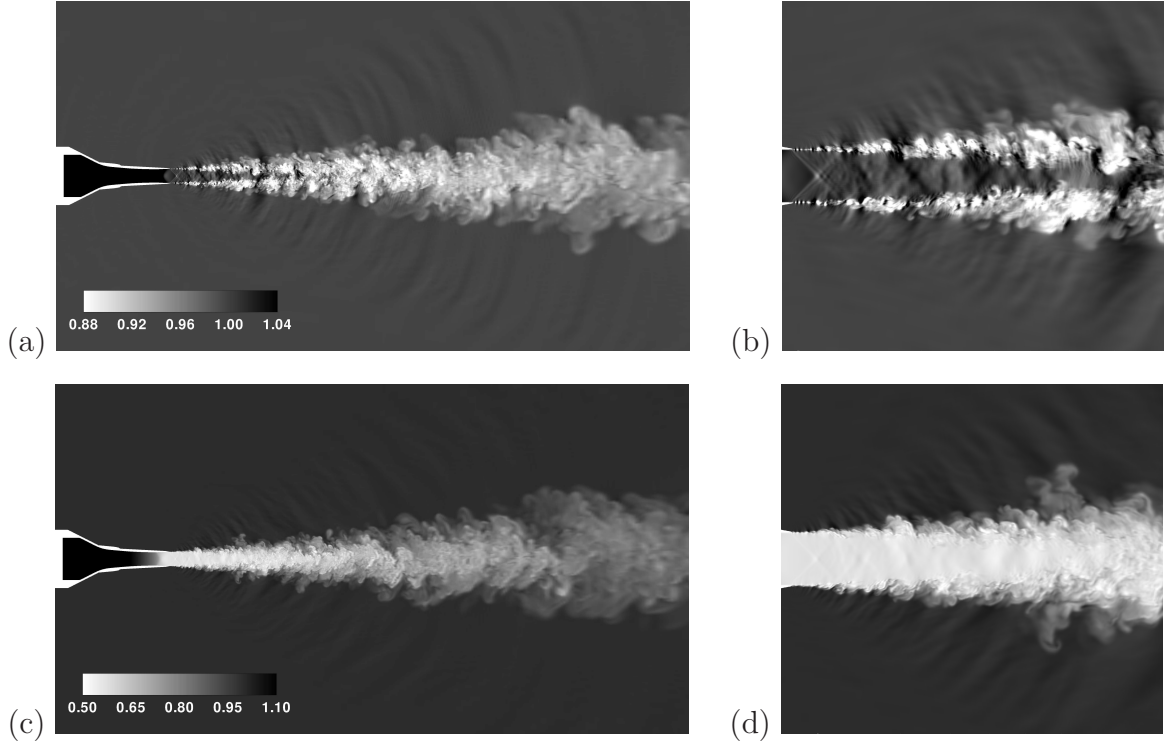


Figure 3: Instantaneous fields of density  $\rho/\rho_\infty$  from simulations S1 (a,b) and S2 (c,d) on the cutting plane  $z = 0$ . Figures (b) and (d) are zooms of figures (a) and (c), respectively. Scale is different for figures (a,b) and (c,d). A color version of the figure can be found in ref. 32 and 44.

First, instantaneous fields of density are displayed in Fig. 3 to show how the jet develops. The jet issues from the nozzle (on the left). As already stated, the mixing layer between the jet and the ambient flow is initially laminar. At approximately  $x = 1D$ , the mixing layer shows strong instabilities that rapidly lead to turbulent transition. Two diameters downstream of the nozzle exit, the mixing layer is turbulent. The scenario is identical for the isothermal jet and the heated jet. Weak shock cells can be observed in the instantaneous density fields. The first cell, in particular, appears clearly. The following ones are more distorted by the turbulent eddies in the flow. Figure 3 also shows the emission of sound, with a strong downstream directivity. Sound wave emission is particularly clear in the isothermal case, due to the narrow density scale used for the figure. In the heated case, Mach waves are clearly emitted from the beginning of the mixing layer (Fig. 3d).

## B. Time-averaged flow data.

Figure 4 shows the comparison of time-averaged velocity field between numerical results and experimental data for both cases. Both time-averaged streamwise velocity  $U$  and root mean square (RMS) streamwise velocity  $u_{rms}$  are plotted. Results are extracted along the centerline ( $r = 0$ , in black in Fig. 4) and along the mixing layer, in front of the lip of the nozzle ( $r = 0.5 D$ , in red in Fig. 4), between  $x = 0$  and  $x = 25 D$ . Along the lip line, LES results are azimuthally averaged. As discussed in appendix B, due to quality issues, data upstream of  $x = 0.25 D$  on the centerline and upstream of  $x = D$  on the lip line had to be discarded. Some differences were seen in the experimental data between results along lines  $y = 0.5 D$  and  $y = -0.5 D$  ( $z = 0$ ). Lip line experimental data displayed in Fig. 4 is the average of the measurements over the two lines (differences between the experimental measurements over lines  $y = 0.5 D$  and  $y = -0.5 D$  can be seen in the appendix B).

The top figures in Fig. 4 focuses on the isothermal case S1. Figure 4(a) shows time-averaged streamwise velocity profiles for S1. The prediction along the lip line is good, while along the centerline, the numerical jet has a potential core slightly shorter than the experimental jet. Defining the end of the potential core as the location where the velocity is 95 % of the jet velocity at the nozzle exit, the potential core in the LES is one diameter shorter than in the experiment. Furthermore, it can be seen in Fig. 4(a) that the intensity of the shocks is smaller in the LES than in the experiment. This is a direct consequence of the pressure mismatch at the nozzle exit between the jet and the ambient. The operating points in the LES are not exactly identical to the experimental ones, but differences are of order of 0.5 %. In addition to this small difference, Bridges and Wernet<sup>33</sup> state how difficult it is to reach fully-expanded conditions, notably by pointing out the sensitivity to boundary layers and nozzle lip thickness. Differences between the LES and the experiment in terms of nozzle boundary layers and flow in the vicinity of the nozzle may also contribute to the differences in the shocks amplitudes.

Turbulent fluctuations in the streamwise direction are reported in Fig. 4(b). The overall trends in the LES follow the experiment. Notably, levels of fluctuations roughly match the experiment. Several discrepancies can however be observed: along the lip line, fluctuations obtained in the LES near the nozzle are obviously higher than the ones in the experiment. Despite the fact that the transition of the mixing layer is rapid in the LES, almost 5 diameters are necessary to recover values of fluctuations similar to the experimental ones. Along the centerline, the rise is earlier than in the experiment, sign of a shorter potential core. The differences between LES and experimental results correspond well to what is found by Bogey and Bailly in the case of LES of initially laminar jets transitioning to turbulence outside the nozzle: thinner initial boundary layers, and velocity fluctuations inside the nozzle would lead to an increase in the potential core, and a decrease in the fluctuation peak along the

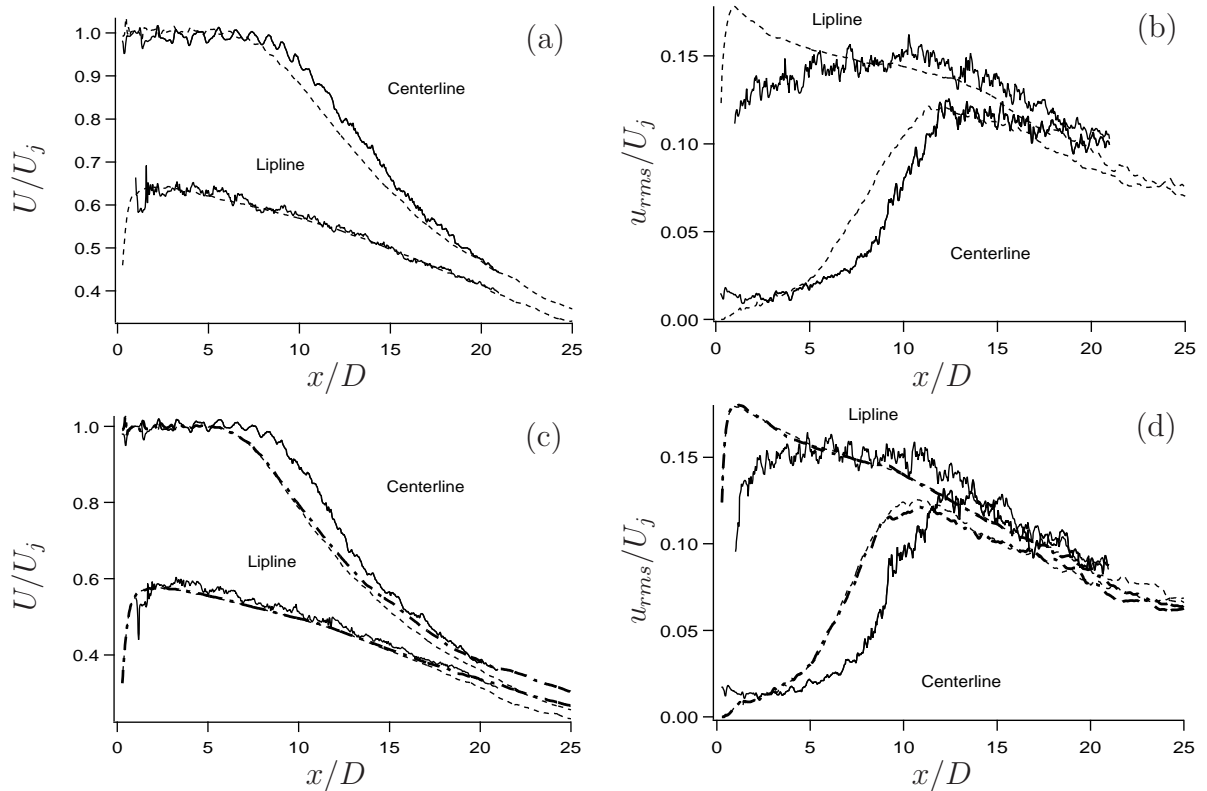


Figure 4: Comparisons between numerical and experimental (—) results along the centerline and a lip line between  $x = 0$  and  $x = 25 D$ . Time-averaged (a) and RMS (b) of streamwise velocity for the unheated case S1 (----), time-averaged (c) and RMS (d) of streamwise velocity for the heated cases S2 (-----) and S3 (- - -).

lip line. Downstream of the peak in the fluctuations level ( $x \approx 13 D$ ), the decrease in fluctuations is more rapid in the LES. As shown by Khalighi *et al.*,<sup>30</sup> the transition region can be shortened by using local refinement in the azimuthal direction, near the nozzle lip. Such a local azimuthal refinement improves both the near-nozzle values of RMS of velocity fluctuations and the length of the potential core.

Results in the heated case are similar (Fig. 4c,d). Experimental trends are reproduced in the LES and levels are generally in good agreement. Shocks amplitude is also larger in the experiment than in the LES (Fig. 4c). However, results show a larger difference of the potential core length between the LES and the experiment (of approximately  $2 D$ ). This results in substantial differences along the centerline, for the time-averaged velocity as well as for the fluctuations. Note however that a decrease in the potential core length (as predicted in the LES) is expected when  $TR$  increases.<sup>34,54</sup> The higher discrepancies between the experiment and the LES in the heated case may also be due to the thicker boundary layer at the exit of the nozzle in the heated case compared with the one in the unheated

(Table 1). Note that despite the improvement of the grid from S2 to S3 downstream of  $x = 11 D$ , no significant difference in the turbulent fluctuation levels is observed between the two simulations. Additional grid sensitivity results are presented in Appendix A for the heated case (Fig. 13): coarse simulation results show that even a 2-million-cell grid (twice as coarse as grid 1&2 in each direction) provides reasonable flow (and noise) results. A good grid resolution yields a shorter laminar-to-turbulent transition in the mixing layer. Turbulence levels are consequently better in the initial part of the mixing layer. In addition, the length of the potential core is longer with better resolution. This grid refinement study is a measure of the quality of the results and confirms that the solution follows the correct trend as the grid becomes finer. This also demonstrates that the good results obtained with the current approach are not entirely tied to a specific choice of resolution.

Radial profiles of time-averaged velocity, fluctuating velocity components  $u_{rms}$ ,  $v_{rms}$  and turbulent shear stress  $uv$  are shown for 4 axial positions in Fig. 5 for the unheated case and Fig. 6 for the heated case. Again, cases S2 and S3 are compared for the heated case. Both figures show the same trends: numerical results are generally in a good agreement with the experiment, in terms of shape of profiles and levels, for all quantities. However, two types of discrepancies can be seen: first, as seen in the former figures, fluctuations near the nozzle are clearly over-estimated due to the laminar-to-turbulent transition. This is visible in particular on  $v_{rms}$  (and  $w_{rms}$ , as shown previously<sup>44</sup>). Differences with the experiment decrease with the axial position of the profiles. Note that this difference may also be due to an under-estimation of the RMS in the experiment. As shown later on velocity spectra, the experimental sample rate is probably insufficient to accurately measure RMS in the near-nozzle region.

Another clear difference is the size of the shear layer. Time-averaged velocity profiles show steeper gradients in the experiment. This is confirmed by the fluctuating velocity profiles, where the radial extent of the shear layer is smaller in the experiment. Refining the grid and decreasing the initial mixing layer thickness would be necessary to improve these features.

What clearly comes out of these results is the importance of the mixing layer development near the nozzle. Note that the thin laminar shear layer in pristine flow (as here) over excites the vortex roll-up and pairing, and spreads more rapidly than its turbulent counterpart. When comparing LES of initially laminar jets to experiments where the flow in the nozzle is most probably turbulent, it is extremely important to obtain a quick transition to turbulence, as shown by Shur, Spalart, Strelets and co-workers.<sup>8,17-20</sup> In the present study, the initial boundary layer momentum thickness is relatively small ( $\delta_\theta \approx 0.002 D$ ) compared to what is usually encountered in the literature. The grid is not sufficient to resolve the flow in the mixing layer (the minimal radial grid step is typically only 4 times smaller than the

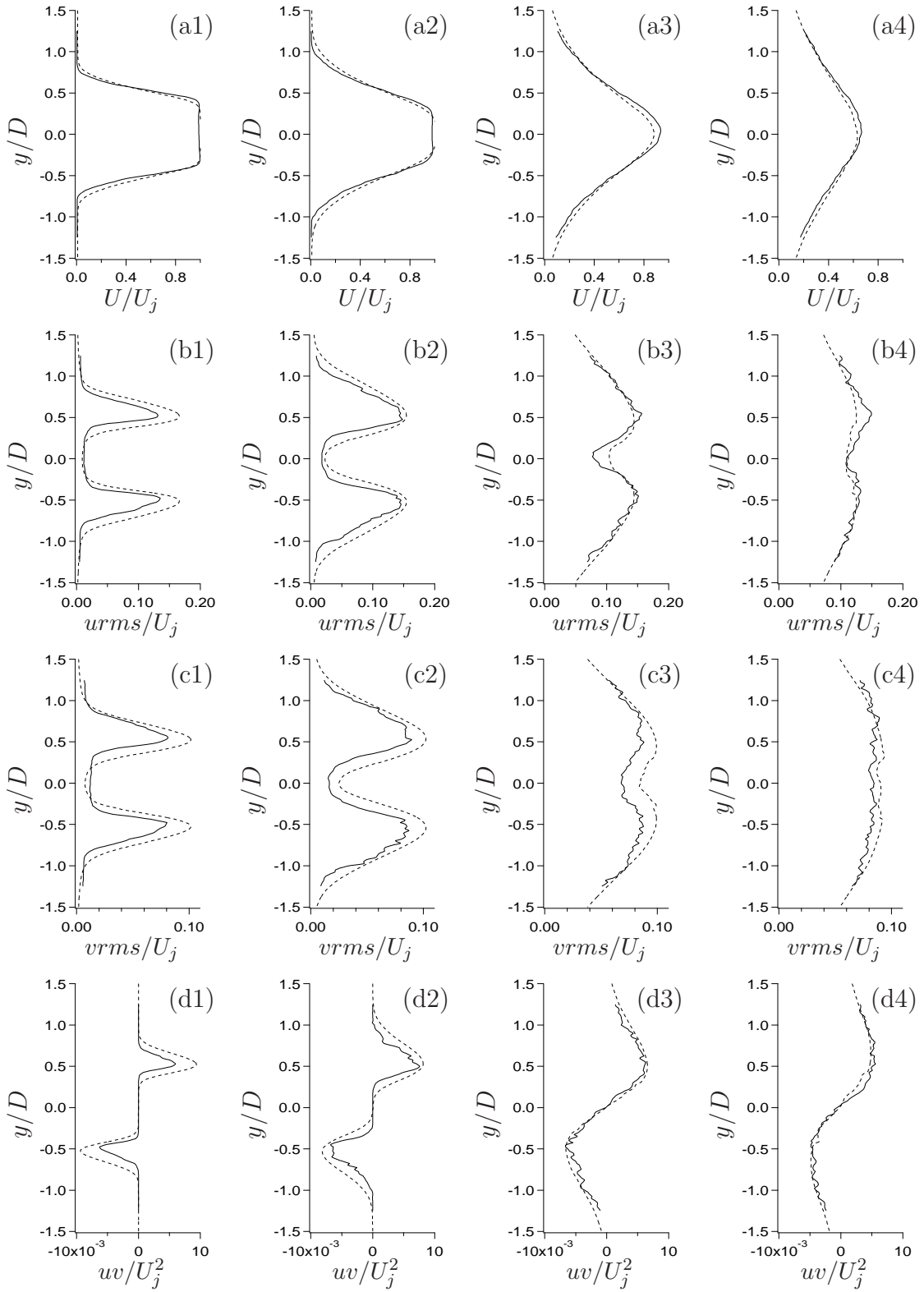


Figure 5: Comparisons between numerical results from S1 (----) and experimental data (—). Radial profiles of time-averaged streamwise velocity (a row), RMS of streamwise (b row) and radial (c row) velocity components and turbulent shear stress  $uv$  (d row) for  $x/D = 2.5, 5, 10, 15$  (columns 1 to 4), at  $z = 0$ .

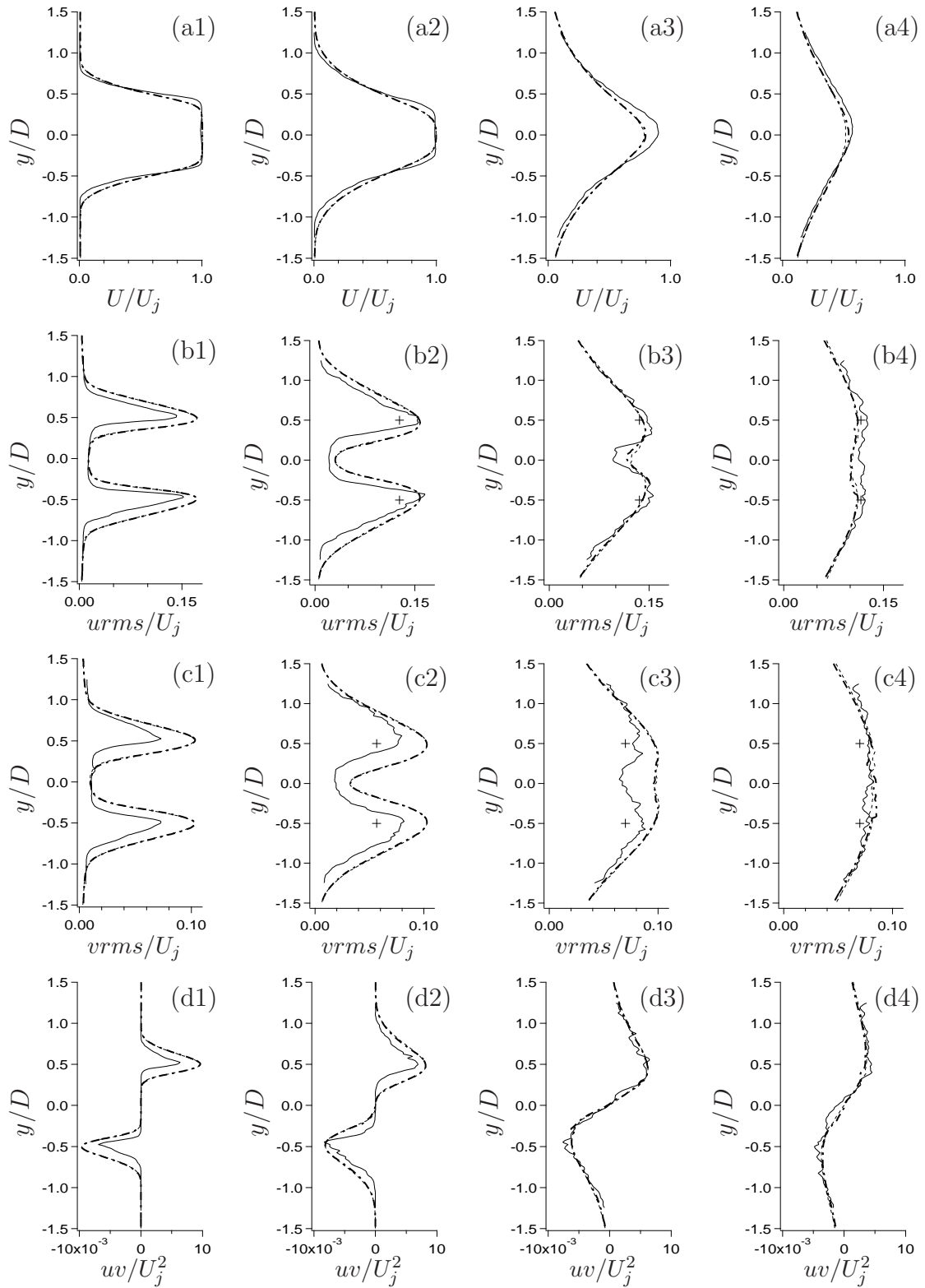


Figure 6: Comparisons between numerical results from S2 (-----), S3 (-.-.-) and experimental data (—). Radial profiles of time-averaged streamwise velocity (a row), RMS of streamwise (b row) and radial (c row) velocity components and turbulent shear stress  $uv$  (d row) for  $x/D = 2.5, 5, 10, 15$  (columns 1 to 4), at  $z = 0$ . Experimental RMS data calculated from the integration of velocity spectra displayed in section V.C are displayed by +.

displacement thickness at the nozzle exit). The transition to turbulence is thus clearly numerical. However, obtaining a quick transition, even unphysical, allows a fair agreement between measurements and simulations.

### C. Velocity spectra

Narrowband velocity spectra in the plume are calculated and compared with experimental measurements. Simulation S3 (heated case) is used. From the experiment, velocity spectra for both streamwise and radial components are available. However, they come from a different experimental run than the one presented in the former section. Velocity spectra are calculated from post-processing PIV fields sampled at 10 kHz. The associated Nyquist Strouhal number is 0.4. Thus the range of frequencies over which numerical and experimental results are both available is restricted to  $St < 0.4$ . Comparison of power spectral densities (PSD) is displayed in Fig. 7, for streamwise velocity (Fig. 7a) and radial velocity (Fig. 7b). Seven locations along the lip line ( $r = 0.5 D$ ) are considered in Fig. 7:  $x = 0.5 D$ ,  $1.25 D$ ,  $2.5 D$ ,  $5 D$ ,  $10 D$ ,  $15 D$  and  $30 D$ . Experimental data were only available for  $x = 5 D$ ,  $10 D$  and  $15 D$  because 1) for the most upstream locations, the time resolution of the experimental measurement is not sufficient to capture the energy-containing fluctuations and 2) last location ( $x = 30 D$ ) is out of the PIV window. PSDs have been shifted to separate the plots: a cumulative shift of  $-5$  dB has been added (results at  $x = 0.5 D$  are not shifted). The first six stations are located in the structured part of the grid. Spectra are azimuthally averaged. Spectra at the last station are measured at  $x = 30 D$ ,  $y = 0.5 D$  and  $z = 0$ , in the unstructured part of the grid.

Figure 7 shows how turbulence develops along the lip line in the LES. At  $x = 0.5 D$ , velocity spectra display high intensities for high frequencies. Traces of the initial mixing layer instability can be observed, with peaks emerging from the spectra. Along the lip line, the PSDs increase at low frequencies and decrease at high frequencies. For  $2.0 \leq St \leq 4.0$ , PSDs are high at the first three locations, then decrease rapidly (a 3dB difference is observed for this range between PSDs at  $x = 2.5 D$  and  $5.0 D$ ). From the spectra, the grid seems sufficient to resolve the noise sources up to  $St = 4$  until  $x = 5 D$  (4). At this station, a change in the slope of the spectra at  $St \approx 4$  (the slope of the spectra measured at  $x = 5 D$  clearly differ at  $St = 3$  and  $St = 5$ ) indicates the dissipation of the turbulent fluctuations by the grid. Finally, at  $x = 30 D$  (7), the grid is not able to sustain turbulent fluctuations for  $St > 0.5$ . This location corresponds to the downstream end of the FWH surface.

The agreement between numerical and experimental spectra is good. Levels are in good agreement and trends are well respected. Spectra are relatively flat at  $x = 5 D$ ,  $r = 0.5 D$  and show a more pronounced slope further from the nozzle. This behavior is obtained both in the experiment and the LES. At  $x = 5 D$ , the radial velocity spectrum from the LES shows the

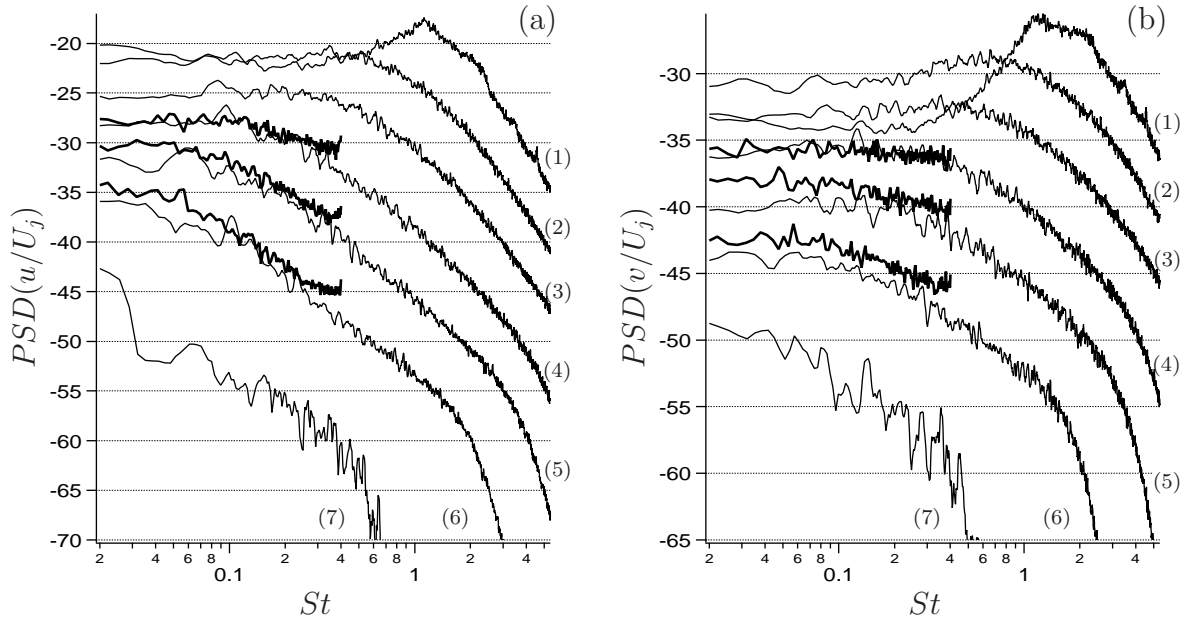


Figure 7: Comparisons between numerical (—) and experimental (—) narrowband power spectral density of streamwise (a) and radial (b) velocity for simulations S3 along the lip line at  $x = 0.5 D$  (1),  $x = 1.25 D$  (2),  $x = 2.5 D$  (3),  $x = 5 D$  (4),  $x = 10 D$  (5),  $x = 15 D$  (6),  $x = 30 D$  (7). A cumulative shift of  $-5$  dB has been added to the PSDs to separate the plots, from  $-5$  dB at  $x = 1.25 D$  (2) to  $-30$  dB at  $x = 30 D$  (7).

power spectral density associated with high-frequency fluctuations is important. To verify how experimental time sampling may impact the measurements, RMS values of velocity fluctuations are computed by integrating the experimental spectra used in the present section and reported in Fig. 6. Differences between the measurements using a sample rate of 10 kHz (+) or 25 kHz (solid lines in Fig. 6) are small for  $u_{rms}$ , but substantial for  $v_{rms}$ , especially near the nozzle. The sample rate (even at 25 kHz) might not be sufficient to obtain the accurate measurements of the radial velocity statistics close to the nozzle.

#### D. Far-field sound

Far-field sound results are compared to experimental measurements. For the unheated (resp. heated) jet, the numerical time sampling allows to obtain data up to  $St = 7$  (resp. 5.4). However, table 3 shows that the grid resolution at the FWH surface location is not sufficient to predict sound for  $St \gtrsim 4$ . The duration of the record enables to capture one period of fluctuations at  $St \approx 0.004$  for S1 and at  $St \approx 0.003$  for S2 and S3. Former tests on the noise post-processing have shown that noise results are not time-converged if statistics are gathered over less than ten periods for a given  $St$ . Hence, noise results are presented for  $0.04 \leq St \leq 4.0$  in S1 and for  $0.03 \leq St \leq 4.0$  in S2 and S3.

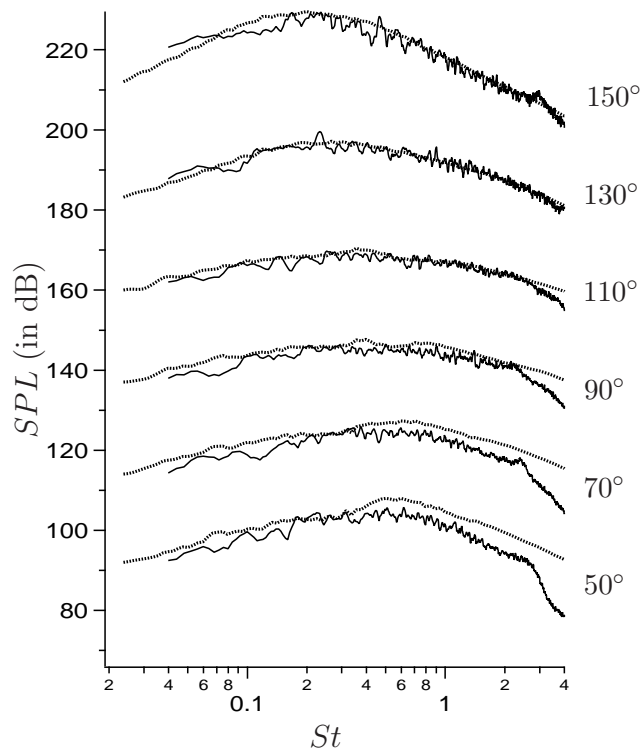


Figure 8: Comparisons of far-field sound narrowband spectra at  $100 D$  between numerical results from S1 (—) and experimental data (.....). Spectra are calculated every  $20^\circ$  from  $50^\circ$  (upstream) to  $150^\circ$  (downstream). Numerical and experimental spectra are staggered by adding a cumulative shift of  $20 \text{ dB}$  for each angle ( $100 \text{ dB}$  are added for angle  $150^\circ$ ).

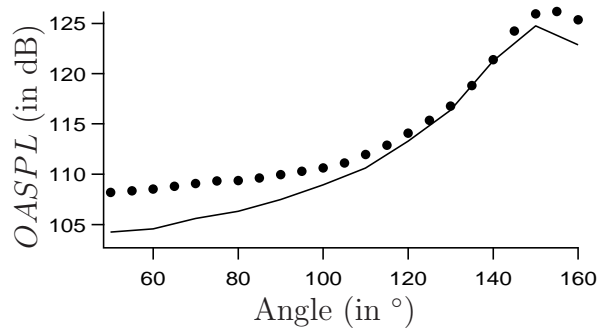


Figure 9: Comparisons of far-field overall sound pressure level at  $100 D$  between numerical results from S1 (—) and experimental data (symbols).

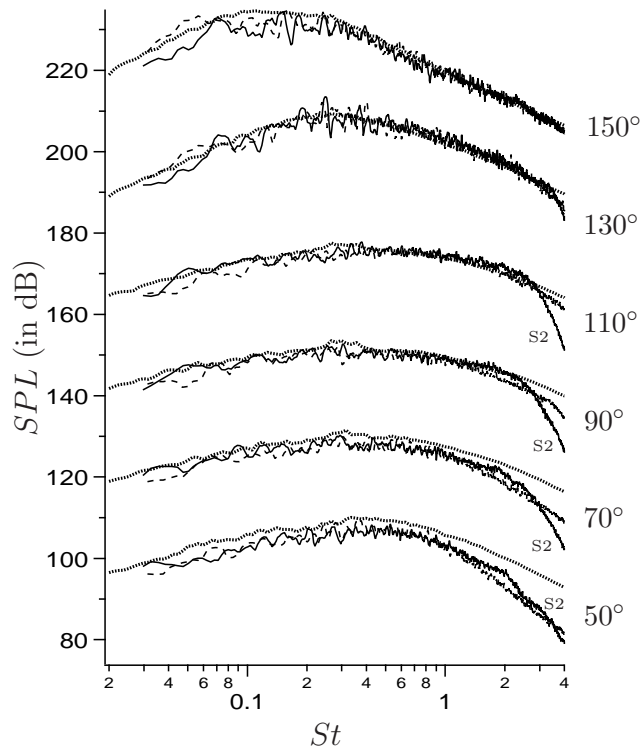


Figure 10: Comparisons of far-field sound narrowband spectra between numerical results from simulations S2 (—) and S3 (----) and experimental data (.....). Spectra are calculated every 20° from 50° (upstream) to 150° (downstream). Numerical and experimental spectra are staggered as in Fig. 8.

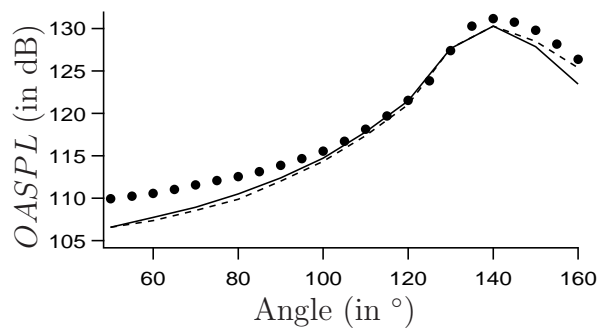


Figure 11: Comparisons of far-field overall sound pressure level at 100  $D$  between numerical results from S2 (—) and S3 (----) and experimental data (symbols).

Narrowband power spectral density of pressure fluctuations at  $100D$  is calculated using the FWH integration method<sup>49</sup> (see § III.E). Far-field sound spectra for case S1 are shown in Fig. 8. The grid resolution appears to be too coarse to obtain reliable sound for  $St > 2$  for upstream locations ( $\theta \leq 90^\circ$ ). A rapid drop in the sound pressure level is observed for high frequencies. Apart from the most upstream location (Fig. 8,  $50^\circ$ ), where sound from the LES is approximately 4 dB lower than in the experiment for  $St > 0.5$ , numerical results are in excellent agreement with the measurements. Levels of sound and peak frequencies are reproduced. As will be shown for the heated case, improvement in the grid resolution at the level of the FWH surface should be able to improve the sound at high frequencies ( $St > 2$ ). However, discrepancies between LES and experimental results for  $0.5 \leq St \leq 2$  at upstream angles are not caused by insufficient grid resolution. Differences are attributed to the presence of stronger shocks in the experiment than in the LES, which induces the present of broadband shock noise (BBSN). In Fig. 8, BBSN appears clearly for the upstream locations. At  $\theta = 50^\circ$ , a clear change in the slope of the experimental spectra can be seen at  $St = 0.3$ . BBSN is even clearer in other data sets obtained at the same test rig: for the same operating point, Bridges and Wernet<sup>33</sup> display another data set than the one displayed here. Probably due to small differences in the inflow conditions, they obtain more substantial broadband shock noise than in the present experimental data set. At a sideline location ( $\theta = 90^\circ$ ) the broadband shock noise dominates for  $St > 0.5$ ,<sup>33</sup> with a peak at  $St = 0.8$ , which matches the data displayed here.

Figure 9 compares the overall sound pressure level in the unheated case S1 with the experiment. Results are reasonable. Errors are higher for upstream angles, where BBSN, which has a strong upstream directivity,<sup>2</sup> is missing in the LES, as shown in the SPL comparisons (Fig. 8). Note that the directivity of the sound is reasonably predicted, even if the peak is not perfectly reproduced.

Far-field sound spectra for cases S2 and S3 (heated jet) are shown in Fig. 10. Observations are the same as for the unheated jet: sound predictions by LES are in good agreement with the experimental measurements. Comparisons improve with the observer angle. As in the unheated case, experimental BBSN is likely to be responsible for the differences in sound predictions in the upstream quadrant for  $St > 0.3$ .

Refining the grid from S2 to S3 leads to better predictions at high frequencies ( $St > 1$ ). This is mainly related to the improvement of radial resolution at the level of the FWH surface. In S2, sound waves are not sufficiently resolved before they reach the FWH surface, as confirmed by additional tests presented in appendix A. It is shown in appendix A that increasing the resolution at the FWH surface improves the high frequency part ( $St > 3$ ) of the spectrum. Differences in the range  $1.5 < St < 2.5$  are likely to be an effect of aliasing errors, also improved by the finer axial resolution in S3 (see appendix A). There are also

some differences in the lowest portion of the spectra  $St < 0.09$ . The reason for changes in the low-frequency noise between S2 and S3 has not been clearly identified. From Fig. 7, and Table 2, the grid cut-off frequency at the downstream end of the FWH surface (where the resolution is the poorest) is measured at  $St \approx 0.5$  in S3 and estimated at  $St \approx 0.2$  in S2. Thus, improvement of the grid in the axial direction is unlikely to be responsible for differences observed in the low-frequency sound, which are probably due to lack of statistical convergence.

Figure 11 compares the overall sound pressure level in the heated cases S2 and S3 with the experimental measurements. Agreement with the experiment is better than the one for the unheated case. Overall, differences between simulations S2 and S3 are small. For S3, in the downstream quadrant, OASPL matches the experimental values with a maximum error of 1 dB for  $90^\circ$ . Errors increase for upstream angles. Maximum error of 3 dB is observed at  $50^\circ$ , where the experimental noise peak, due to BBSN, is not reproduced in the LES.

Note that the typical Mach waves identified visually in Fig. 3 in the density fields are not responsible for the peak jet noise. These waves, generated in the first diameters of the jet, have a higher frequency signature. Waves corresponding to the peak noise frequency ( $St \approx 0.25$ ) have a wavelength of order of  $2.5 D$ . The wavelength of the typical Mach waves seen on instantaneous solutions is around  $1.0 D$  ( $St \approx 0.55$ ). The direction of radiation of the Mach waves is oriented at an angle of approximately  $40^\circ$  to the axis.

## E. Near-field sound

Comparisons of the sound in the near field have been undertaken in heated case, for which experimental data was available. Near-field sound was computed directly from simulation S3 by extracting the signal from the LES and also using the FWH integration with the same surface as for the far-field sound. Spectra are extracted (or calculated) at 64 azimuthal stations, then averaged to smooth the data. Results are displayed in Fig. 12. Experimental data is shown at eight locations, at  $r = 3 D$  and  $x = 10.7 D, 13.7 D, 16.7 D, 19.7 D$  and at  $r = 5 D$  and  $x = 13.15 D, 16.15 D, 19.15 D, 22.15 D$ . Note that the experimental data displayed here has been measured for  $TR = 1.665$  instead of  $TR = 1.755$  in the LES. The experimental sound pressure levels have been calculated directly from pressure time signals measured in the near field. The exact same algorithm (windowing, smoothing) has been used to compute the experimental and the computational sound levels. Figure 12 shows how the near-field sound spectrum changes with the axial location. At  $r = 3 D$ , the noise peak in the experimental data changes from  $St \approx 0.5$  to  $St \approx 0.02$  between  $x = 10.7 D$  and  $19.7 D$  (Fig. 12a to d). The same trend is observed at  $r = 5 D$ , the peak frequency decreasing from  $St \approx 0.35$  to  $St \approx 0.012$  with the axial distance (Fig. 12e to h).

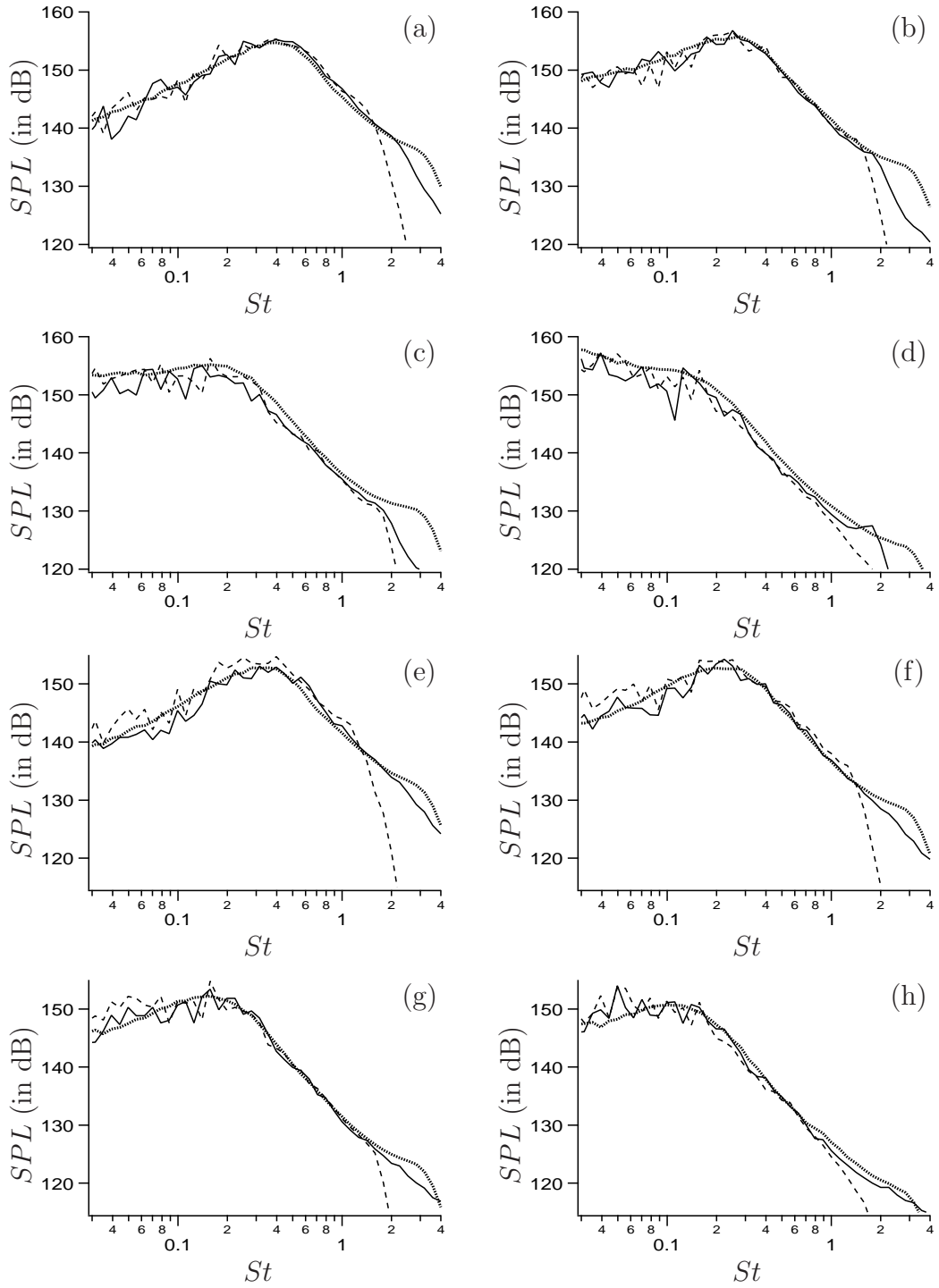


Figure 12: Near-field sound pressure levels at  $r = 3D$  (a-d) and  $r = 5D$  (e-h). Comparison of numerical results directly extracted from simulation S3 (----), using S3 and FWH integration (—) and experimental measurements (.....) at  $r = 3D$  and  $x = 10.7D$  (a),  $x = 13.7D$  (b),  $x = 16.7D$  (c),  $x = 19.7D$  (d) and at  $r = 5D$  and  $x = 13.15D$  (e),  $x = 16.15D$  (f),  $x = 19.15D$  (g),  $x = 22.15D$  (h). Numerical results have been empirically shifted in the axial direction by  $+4D$ .

First, the accuracy of the FWH prediction is verified by comparison with the data directly extracted from the LES. FWH and direct noise calculations significantly differ only for high frequencies. Direct measurement is plagued by the numerical dissipation of the high-frequency sound waves propagating outside the FWH surface, where the grid is coarser. Numerical results are similar to the experimental measurements, but only when shifted by  $+4D$  in the axial direction. This shift has been determined empirically. It has been found to be accurate both at  $r = 3D$  and  $r = 5D$ . It is thought to be the result of two differences between the experiment and the calculation: the temperature ratio, as already stated, and the short potential core obtained in this heated jet simulation. However, the good agreement between the experiment and the simulation once shifted is striking. Levels match and the evolution of the peak frequency and the shape of the spectra with the axial position are well reproduced.

## VI. Conclusion

The present LES effort uses a numerical scheme with minimal dissipation operators, combined with an explicit subgrid-scale model for the scales not captured by the grid and a shock-capturing scheme applied to deal with discontinuities introduced by the presence of shocks. Results show that the combination is accurate enough to reproduce the major trends observed in experiments for the flow and the noise of almost perfectly-expanded supersonic jets. Moreover, quantitative comparisons with experimental data are obtained. This has been demonstrated both for the flow results and the noise in an unheated jet and a heated jet, with minimal pressure mismatch. Relying on unstructured second-order schemes is not the usual option chosen to perform large-eddy simulations for aeroacoustic applications. It is thus of main importance to show the ability of the method to provide results in line with the state of the art in the LES for jet noise literature. The experimental database generated at NASA Glenn Research Center enabled an extensive validation of the simulations. Regarding this aspect, this work is rare, as it presents systematic comparisons with experiments on the main flow, fluctuating quantities, velocity spectra, narrowband near- and far-field sound. Flow results correspond to what is usually seen in the literature. On the other hand, noise results are superior to most of the results available in studies focusing on supersonic jet noise. Compared to the experiment, the main discrepancies observed here are the under-estimation of the potential core length and the under-estimation of the high-frequency noise due to the limited range of scales resolved in the LES. These features are classical differences between LES and experiments, and are expected to improve with the grid resolution. Part of the differences in the predicted sound is also attributed to the presence of stronger shocks in the experiment, responsible for the generation of non-negligible broadband shock noise.

Overall, in terms of validation of LES against experiments, the present results are as good as many obtained by using structured solvers and high-order schemes.

## VII. Acknowledgements

J. Bridges and J. De Bonis, NASA Glenn Research Center, are gratefully acknowledged for their help and for sharing the experimental database. This work is supported by the Supersonics element of NASA Fundamental Aeronautics Program under grant number NNX07AC94A. For the computations, this research was supported in part by the National Science Foundation through TeraGrid resources (project CTS090081) provided by the National Institute for Computational Sciences on the Kraken supercomputer and by the United States Department of Energy through Predictive Science Academic Alliance Program (PSAAP) resources provided by Lawrence Livermore National Laboratory on the Hera supercomputer.

## VIII. Appendix

### A. About grid sensitivity

More information about the grid sensitivity analysis is provided in this appendix, presenting additional results on a coarser grid for the heated case. The grid used for simulation S2 is coarsened twice in each direction, to obtain a grid of 2.1 million cells. The heated case is run in the exact same condition as S2. This coarse simulation is referred to as S2c. As shown by time-averaged flow data (Fig. 13) and far-field sound spectra (Fig. 14), lack of resolution is responsible for enhanced velocity fluctuations near the nozzle, shortened potential core, and important loss of high frequency contributions to far-field sound. However, a very coarse grid still provides a good general picture of the flow and the low-frequency sound.

To better analyze the difference between S2 and S3, additional results are presented, over another grid. Simulation S2r is run over a 20-million cell grid having the same resolution as S2 in the axial direction and the same resolution as S3 in the radial direction. Narrowband far-field sound spectra at high frequencies are displayed in Fig. 15. The only difference between simulations S2 and S2r is the radial resolution between the turbulent region and the FWH surface. In S2r, the radial resolution at the FWH surface corresponds to the one of S3, detailed by Table 3. Figure 15 shows that this difference explains the improvement of the high-frequency sound predictions between S2 and S3. S2r and S3 results are almost identical at high frequencies. The axial refinement of the grid between S2r (and S2) and S3 has a marginal effect, visible only for  $\theta = 50^\circ$  and  $\theta = 70^\circ$ . At these locations, sound predictions slightly differ in the range  $1.5 < St < 2.5$ , probably due to aliasing of high-frequency sound

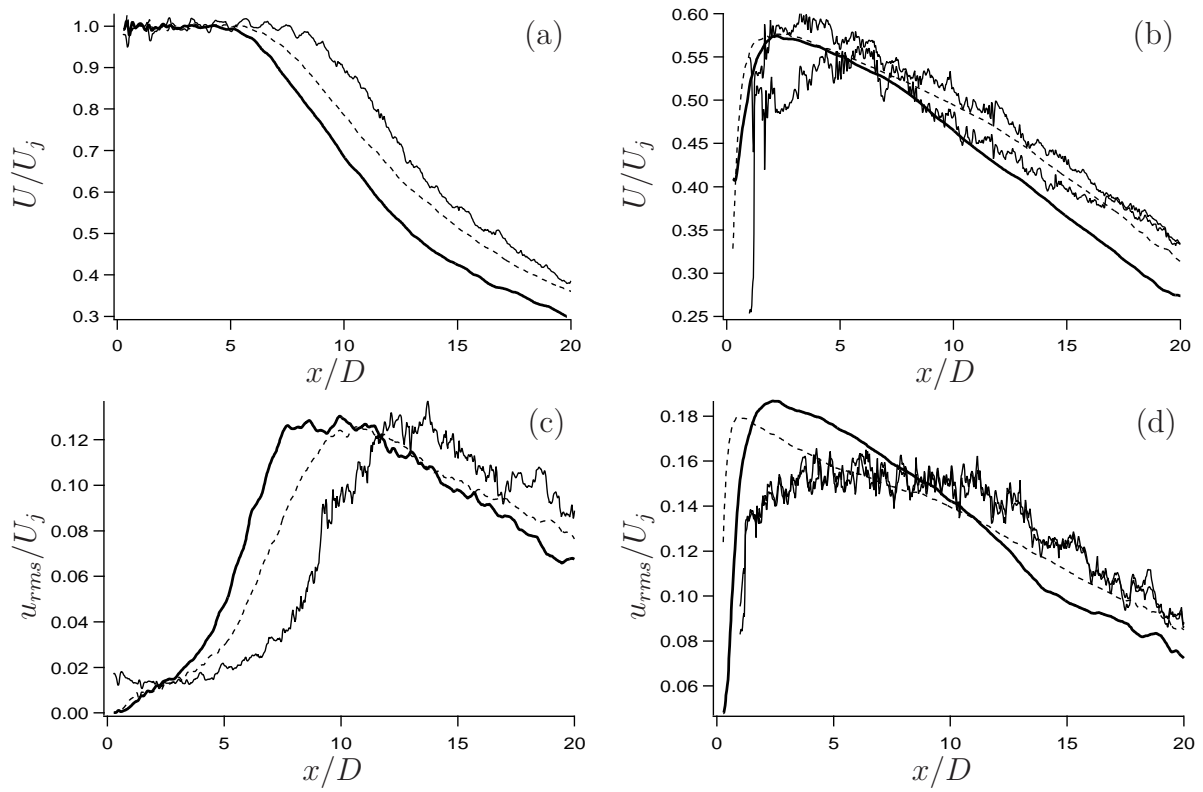


Figure 13: Comparisons between numerical results from S2 (----) and S2c (—) and experimental data (—) along the centerline (a,c) and a lip line (b,d), between  $x = 0$  and  $x = 20 D$ : time-averaged (a,b) and RMS (c,d) of streamwise velocity. Experimental data along the lip line are measured along  $y = 0.5 D$  and  $y = -0.5 D$  and both displayed (b,d) using a solid line.

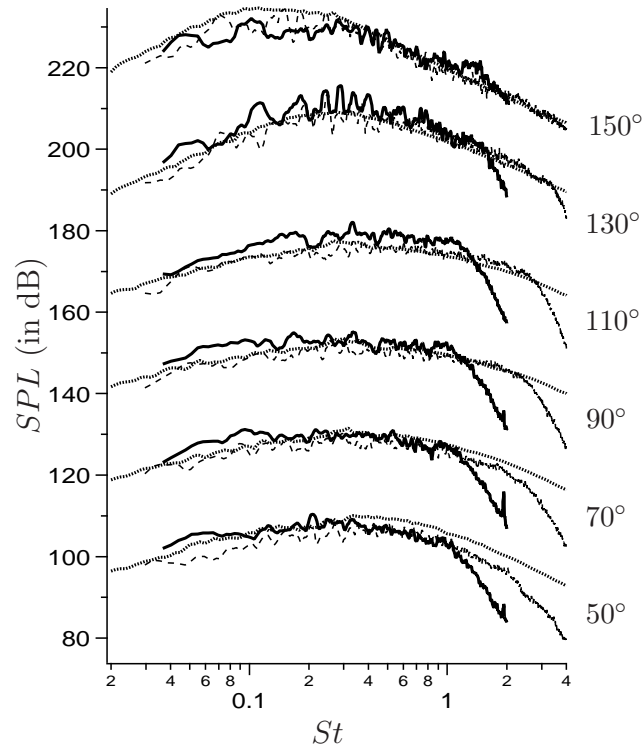


Figure 14: Comparisons of far-field sound narrowband spectra between experimental measurements (.....) and numerical results from simulations S2 (—) and S2c (---), from 50° (upstream) to 150° (downstream). Numerical and experimental spectra are staggered by adding a cumulative shift of 20 dB for each angle (100 dB are added for angle 150°). For sake of legibility, spectra of the S2c case are shown up to  $St = 2$  to avoid mixing staggered graphs at different angles.

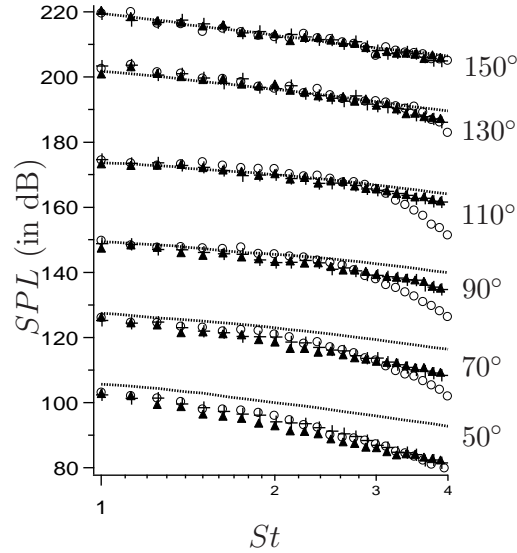


Figure 15: Comparisons of far-field high-frequency sound between experiment (.....) and numerical results from simulations S2 ( $\circ$ ), S3 ( $\blacktriangle$ ) and S2r ( $+$ ), from  $50^\circ$  (upstream) to  $150^\circ$  (downstream). Numerical and experimental spectra are staggered by adding a cumulative shift of 20 dB for each angle (100 dB are added for angle  $150^\circ$ ). Narrowband spectra from simulations are displayed with symbols, every  $St=0.12$  to be able to differentiate the results.

because of dispersion errors.

## B. Comments about the experimental velocity measurements

Experimental data was measured over the cutting plane  $z = 0$ . Lip line data is available along two lines,  $y = 0.5 D$  and  $y = -0.5 D$ . Experimental measurements along the two lines differ, as shown in Fig. 13(b,d). Indeed, the jets in the experiment seem to slightly deviate from the centerline. This is confirmed by the radial profiles in Fig. 5(a3-a5) and Fig. 6(a3-a5), where the maximum of streamwise velocity is located slightly above  $y = 0$ . Time-averaged measurements along the two lip lines are rather different. On the contrary, the RMS of streamwise velocity is almost identical along the two lines. This is expected, as the radial gradient of time-averaged streamwise velocity is high at  $r = 0.5 D$ , while the gradient of the RMS of velocity fluctuations is small. Note also that experimental measurements in the range  $1 D \leq x \leq 2 D$  are quite uncertain. The quality index measured in the experiment (number of the usable PIV samples over the total number of samples<sup>55</sup>) is approximately 0.5 in this zone.

## References

- <sup>1</sup>Bodony, D. J. and Lele, S. K., “Current Status of Jet Noise Predictions Using Large-Eddy Simulation,” *AIAA Journal*, Vol. 46, No. 3, 2008, pp. 364–380.
- <sup>2</sup>Tam, C. K. W., “Supersonic jet noise,” *Annual Review of Fluid Mechanics*, Vol. 27, 1995, pp. 17–43.
- <sup>3</sup>Tam, C. K. W., “Jet noise: since 1952,” *Theoretical and Computational Fluid Dynamics*, Vol. 10, 1998, pp. 393–405.
- <sup>4</sup>Bogey, C. and Bailly, C., “Investigation of downstream and sideline subsonic jet noise using Large Eddy Simulation,” *Theoretical and Computational Fluid Dynamics*, Vol. 20, No. 1, 2006, pp. 23–40.
- <sup>5</sup>Gamet, L. and Estivalezes, J.-L., “Application of Large-Eddy Simulations and Kirchhoff Method to Jet Noise Prediction,” *AIAA Journal*, Vol. 36, No. 12, 1998, pp. 2170–2178.
- <sup>6</sup>Morris, P. J., Long, L. N., Scheidegger, T. E., and Boluriaan, S., “Simulations of supersonic jet noise,” *International Journal of Aeroacoustics*, Vol. 1, No. 1, 2002, pp. 17–41.
- <sup>7</sup>Bogey, C. and Bailly, C., “Computation of a high Reynolds number jet and its radiated noise using large eddy simulation based on explicit filtering,” *Computers and Fluids*, Vol. 35, 2006, pp. 1344–1358.
- <sup>8</sup>Shur, M. L., Spalart, P. R., and Strelets, M. K., “Noise prediction for increasingly complex jets. Part I: Methods and tests,” *International Journal of Aeroacoustics*, Vol. 4, No. 3&4, 2005, pp. 213–246.
- <sup>9</sup>Lo, S.-C., Blaisdell, G. A., and Lyrintzis, A. S., “Numerical Simulation of Supersonic Jet Flows and their Noise. AIAA 2008-2970,” *14th AIAA/CEAS Aeroacoustics Conference, Vancouver, CANADA, 5-7 May 2008*, 2008.
- <sup>10</sup>Xia, H., Tucker, P. G., and Eastwood, S., “Large-eddy simulations of chevron jet flows with noise predictions,” *International Journal of Heat and Fluid Flow*, Vol. 30, 2009, pp. 1067–1079.
- <sup>11</sup>Uzun, A., Lyrintzis, A. S., and Blaisdell, G. A., “Coupling of integral acoustics methods with LES for jet noise prediction,” *International Journal of Aeroacoustics*, Vol. 3, No. 4, 2004, pp. 297–346.
- <sup>12</sup>Bodony, D. J. and Lele, S. K., “On using large-eddy simulation for the prediction of noise from cold and heated turbulent jets,” *Physics of Fluids*, Vol. 17, 2005.
- <sup>13</sup>Andersson, N., L.-E., E., and Davidson, L., “Large-Eddy Simulation of Subsonic Turbulent Jets and Their Radiated Sound,” *AIAA Journal*, Vol. 43, No. 9, 2005, pp. 1899–1912.
- <sup>14</sup>Burak, M. O., Eriksson, L.-E., Munday, D., Gutmark, E., and Prisell, E., “Experimental and Numerical Investigation of a Supersonic C-D Nozzle. AIAA 2009-3252,” *15th AIAA/CEAS Aeroacoustics Conference, Miami, Florida, USA, 11-13 May 2009*, 2009.
- <sup>15</sup>Liu, J., Kailasanath, K., Ramamurti, R., Munday, D., Gutmark, E., and Lohner, R., “Large-Eddy Simulations of a Supersonic Jet and Its Near-Field Acoustic Properties,” *AIAA Journal*, Vol. 47, No. 8, 2009, pp. 1849–1864.
- <sup>16</sup>Wang, M., Freund, J. B., and Lele, S. K., “Computational Prediction of Flow-Generated Sound,” *Annual Review of Fluid Mechanics*, Vol. 38, 2006, pp. 483–512.
- <sup>17</sup>Shur, M. L., Spalart, P. R., and Strelets, M. K., “Noise prediction for increasingly complex jets. Part II: Applications,” *International Journal of Aeroacoustics*, Vol. 4, No. 3&4, 2005, pp. 247–266.
- <sup>18</sup>Shur, M. L., Spalart, P. R., Strelets, M. K., and Garbaruk, A. V., “Analysis of jet-noise-reduction concepts by large-eddy simulation,” *International Journal of Aeroacoustics*, Vol. 6, No. 3, 2007, pp. 243–285.
- <sup>19</sup>Spalart, P. R., Shur, M. L., and Strelets, M. K., “Identification of Sound Sources in Large-Eddy

Simulations of Jets. AIAA 2007-3616,” *13th AIAA/CEAS Aeroacoustics Conference, Rome, ITALY, 21-23 May 2007*, 2007.

<sup>20</sup>Viswanathan, K., Shur, M. L., Spalart, P. R., and Strelets, M. K., “Flow and Noise Predictions for Single and Dual-Stream Beveled Nozzles,” *AIAA Journal*, Vol. 46, No. 3, 2008, pp. 601–626.

<sup>21</sup>Fureby, C., Henriksson, M., Parmhed, O., Sjökvist, L., and Tegnér, J., “CFD Predictions of Jet Engine Exhaust Plumes. AIAA 2008-3727,” *38th AIAA Fluid Dynamics Conference and Exhibit, Seattle, Washington, USA, June 23–26, 2008*, 2008.

<sup>22</sup>Eastwood, S., Tucker, P., Xia, H., Dunkley, P., and Carpenter, P., “Large-Eddy Simulations and Measurements of a Small-Scale High-Speed Coflowing Jet,” *AIAA Journal*, Vol. 48, No. 5, 2010, pp. 963–974.

<sup>23</sup>Eastwood, S., Tucker, P., and Xia, H., “High-Performance Computing in Jet Aerodynamics,” *Parallel Scientific Computing and Optimization*, edited by S. N. York, Vol. 27 of *Springer Optimization and Its Applications*, 2009, pp. 193–206.

<sup>24</sup>Vuillot, F., Lupoglazoff, N., and Huet, M., “Effect of chevrons on double stream jet noise from hybrid CAA computations. AIAA 2011-1154,” *49th AIAA Aerospace Sciences Meeting Including The New Horizons Forum and Aerospace Exposition, Orlando, Florida, 4-7 January 2011*, 2011.

<sup>25</sup>Lupoglazoff, N., Rahier, G., and Vuillot, F., “Application of the CEDRE unstructured flow solver to jet noise computations,” *EUROPEAN CONFERENCE FOR AEROSPACE SCIENCES (EUCASS)*, 2005.

<sup>26</sup>Bodard, G., Bailly, C., and Vuillot, F., “Matched hybrid approaches to predict jet noise by using Large-Eddy Simulation. AIAA 2009-3316,” *15th AIAA/CEAS Aeroacoustics Conference, Miami, Florida, USA, 11-13 May 2009*, 2009.

<sup>27</sup>Roe, P. L., “Approximate Riemann solvers, parameter vectors and difference schemes,” *Journal of Computational Physics*, Vol. 43, 1981, pp. 357–372.

<sup>28</sup>Liu, J., Kailasanath, K., Ramamurti, R., Munday, D., and Gutmark, E., “Large-Eddy Simulations of Imperfectly Expanded Jets from a Chevron Nozzle. AIAA 2009-3192,” *15th AIAA/CEAS Aeroacoustics Conference, Miami, Florida, USA, 11-13 May 2009*, 2009.

<sup>29</sup>Ham, F. E., Sharma, A., Shoeybi, M., Lele, S. K., and Moin, P., “Noise Prediction from Cold High-Speed Turbulent Jets Using Large-Eddy Simulation. AIAA 2009-9,” *47th AIAA Aerospace Sciences Meeting Including The New Horizons Forum and Aerospace Exposition, Orlando, Florida, 5-8 January 2009*, 2009.

<sup>30</sup>Khalighi, Y., Ham, F., Moin, P., Lele, S. K., Colonius, T., Schlinker, R. H., Reba, R. A., and Simonich, J. C., “Unstructured large eddy simulation technology for prediction and control of jet noise,” *Proceedings of ASME Turbo Expo 2010: Power for Land, Sea and Air IGTI 2010 June 14-18, 2010, Glasgow, UK*, 2010.

<sup>31</sup>Khalighi, Y., Nichols, J. W., Ham, F., Lele, S. K., and Moin, P., “Unstructured Large Eddy Simulation for Prediction of Noise Issued from Turbulent Jets in Various Configurations,” *17th AIAA/CEAS Aeroacoustics Conference, Portland, Oregon, USA, 6-8 June 2011*, 2011.

<sup>32</sup>Shoeybi, M., *A hybrid implicit-explicit method for the LES of compressible flows on unstructured grids*, Ph.D. thesis, Department of Mechanical Engineering. Stanford University, 2010.

<sup>33</sup>Bridges, J. and Wernet, M. P., “Turbulence Associated with Broadband Shock Noise in Hot Jets, AIAA 2008-2834,” *14th AIAA/CEAS Aeroacoustics Conference, Vancouver, CANADA, 5-7 May 2008*, 2008.

<sup>34</sup>Bridges, J., “Effect of Heat on Space-Time Correlations in Jets. AIAA 2006-2534,” *12th AIAA-CEAS Aeroacoustics Conference, Cambridge, Massachusetts, May 8-10, 2006*, 2006.

- <sup>35</sup>Bridges, J. and Wernet, M. P., “Establishing Consensus Turbulence Statistics for Hot Subsonic Jets. AIAA 2010-3751,” *16th AIAA/CEAS Aeroacoustics Conference, Stockholm, Sweden, 7-9 June 2010*, 2010.
- <sup>36</sup>Shoeybi, M., Svärd, M., Ham, F. E., and Moin, P., “An adaptive implicit–explicit scheme for the DNS and LES of compressible flows on unstructured grids,” *Journal of Computational Physics*, Vol. 229, No. 17, 2009, pp. 5944–5965.
- <sup>37</sup>Nordström, J., Forsberg, K., and Adamsson, C. Eliasson, P., “Finite volume methods, unstructured meshes and strict stability for hyperbolic problems,” *Applied Numerical Mathematics*, Vol. 45, 2003, pp. 453–473.
- <sup>38</sup>Svärd, M., Carpenter, M. W., and Nordström, J., “A stable high-order finite difference scheme for the compressible Navier–Stokes equations, far-field boundary conditions,” *Journal of Computational Physics*, Vol. 225, 2007, pp. 1020–1038.
- <sup>39</sup>Svärd, M. and Nordström, J., “A stable high-order finite difference scheme for the compressible Navier–Stokes equations. No-slip wall boundary conditions,” *Journal of Computational Physics*, Vol. 227, 2008, pp. 4805–4824.
- <sup>40</sup>Moin, P., Squires, K., Cabot, W., and Lee, S., “A dynamic subgrid-scale model for compressible turbulence and scalar transport,” *Physics of Fluids A*, Vol. 3, No. 11, 1991, pp. 2746–2757.
- <sup>41</sup>Lilly, D. K., “A proposed modification of the Germano sub-grid closure method,” *Physics of Fluids A*, Vol. 4, No. 3, 1992, pp. 633–635.
- <sup>42</sup>Svärd, M., Gong, J., and Nordström, J., “Stable artificial dissipation operators for finite volume schemes on unstructured grids,” *Applied Numerical Mathematics*, Vol. 56, 2006, pp. 1481–1490.
- <sup>43</sup>Mittal, R. and Moin, P., “Suitability of upwind biased schemes for large-eddy simulation of turbulent flows,” *AIAA Journal*, Vol. 35, No. 8, 1997, pp. 1415–1417.
- <sup>44</sup>Mendez, S., Shoeybi, M., Sharma, A., Ham, F. E., Lele, S. K., and Moin, P., “Large-Eddy Simulations of Perfectly-Expanded Supersonic Jets: Quality Assessment and Validation. AIAA 2010-271,” *48th AIAA Aerospace Sciences Meeting Including The New Horizons Forum and Aerospace Exposition, Orlando, Florida, 4-7 January 2010*, 2010.
- <sup>45</sup>Nagarajan, S., Lele, S. K., and Ferziger, J. H., “A robust high-order compact method for large eddy simulation,” *Journal of Computational Physics*, Vol. 191, No. 2, 2003, pp. 392–419.
- <sup>46</sup>Cook, A. W. and Cabot, W. H., “Hyperviscosity for shock–turbulence interactions,” *Journal of Computational Physics*, Vol. 203, 2005, pp. 379–385.
- <sup>47</sup>Mani, A., Larsson, J., and Moin, P., “Suitability of artificial bulk viscosity for large-eddy simulation of turbulent flows with shocks,” *Journal of Computational Physics*, Vol. 228, No. 19, 2009, pp. 7368–7374.
- <sup>48</sup>Ffowcs Williams, J. E. and Hawkings, D. L., “Sound generation by turbulence and surface in arbitrary motion,” *Philosophical Transactions of the Royal Society of London*, Vol. 264, 1969, pp. 321–342.
- <sup>49</sup>Mendez, S., Sharma, A., Shoeybi, M., and Lele, S. K., “Post-processing of large-eddy simulations for jet noise predictions,” *Annual Research Briefs. Center for Turbulence Research, Stanford University*, 2009.
- <sup>50</sup>Spalart, P. R. and Shur, M. L., “Variants of the Ffowcs Williams–Hawkings equation and their coupling with simulations of hot jets,” *International Journal of Aeroacoustics*, Vol. 8, No. 5, 2009, pp. 477–492.
- <sup>51</sup>Morfey, C. L. and Wright, M. C. M., “Extensions of Lighthill’s acoustic analogy with application to computational aeroacoustics,” *Proceedings of the Royal Society of London. Series A*, Vol. 463, 2007, pp. 2101–2127.

<sup>52</sup>Uzun, A. and Hussaini, M. Y., “High Frequency Noise Generation in the Near-Nozzle Region of a Jet, AIAA 2006-2499,” *12th AIAA-CEAS Aeroacoustics Conference, Cambridge, Massachusetts, May 8-10, 2006*, 2006.

<sup>53</sup>Bogey, C. and Bailly, C., “Influence of nozzle-exit boundary-layer conditions on the flow and acoustic fields of initially laminar jets,” *Journal of Fluid Mechanics*, Vol. 663, 2010, pp. 507–538.

<sup>54</sup>Witze, P. O., “Centerline Velocity Decay of Compressible Free Jets,” *AIAA Journal*, Vol. 12, No. 4, 1974, pp. 417–418.

<sup>55</sup>Wernet, M. P., “Temporally resolved PIV for space–time correlations in both cold and hot jet flows,” *Measurements Science and Technology*, Vol. 18, 2007, pp. 1387–1403.